

Temperature and doping dependence of normal state spectral properties in a two-orbital model for ferropnictides

J. D. Querales Flores,^{1,2} C. I. Ventura,^{1,3} R. Citro⁴ and J.J. Rodríguez-Núñez⁵

¹*Centro Atómico Bariloche-CNEA and CONICET,*

Av. Bustillo 9500, R8402AGP Bariloche, Argentina

²*Instituto Balseiro, Univ. Nac. de Cuyo and CNEA, 8400 Bariloche, Argentina*

³*Sede Andina, Univ. Nac. de Río Negro, 8400 Bariloche, Argentina*

⁴*Dipartimento di Fisica “E.R. Caianiello” and CNR-SPIN, Università degli Studi di Salerno, I-84084 Fisciano, Italy. and*

⁵*Lab. SUPERCOMP, Departamento de Física – FACYT, Universidad de Carabobo, 2001 Valencia, Venezuela.*

(Dated: March 2, 2024)

Using a second-order perturbative Green’s functions approach we determined the normal state spectral function $A(\vec{k}, \omega)$ employing a minimal model for ferropnictides. Used before to study magnetic fluctuations and superconducting properties, it includes the two effective bands related to Fe-3d orbitals proposed by S.Raghu et al. [Phys. Rev. B 77, 220503 (R) (2008)], and local intra- and inter-orbital correlations for the effective orbitals. Here, we focus on the normal state electronic properties, in particular the temperature and doping dependence of the total density of states, $A(\omega)$, and of $A(\vec{k}, \omega)$ in different Brillouin zone regions, comparing them with existing angle resolved photoemission spectroscopy (ARPES) and theoretical results. We obtain an asymmetric effect of electron and hole doping, quantitative agreement with the experimental chemical potential shifts, as well as spectral weight redistributions near the Fermi level with temperature consistent with the available experiments. In addition, we predict a non-trivial dependence of $A(\omega)$ with temperature, exhibiting clear renormalization effects by correlations. Interestingly, investigating the origin of this predicted behaviour by analyzing the evolution with temperature of the k-dependent self-energy obtained in our approach, we could identify a number of Brillouin zone points, not probed by ARPES yet, where the largest non-trivial effects of temperature on the renormalization are predicted for the parent compounds.

PACS numbers: 71.10.-w, 71.10.Fd, 71.20.-b, 71.20.Gj

I. INTRODUCTION

In 2008, the discovery of superconductivity in $\text{LaFeAsO}_{1-x}\text{F}_x$, with transition temperature $T_c = 26$ K at $x \gtrsim 0.05$ doping,¹ prompted great interest in the experimental and theoretical study of iron-based superconductors. LaOFeAs -like compounds, denoted the 1111-ferropnictide family, served as starting point and were followed rapidly by the discovery of similar electronic properties in a series of other iron-based families of compounds. In the meantime many new superconductors have been found, all of them including quasi-two dimensional(2D) layers with a square-lattice array of Fe ions.^{2,3} A vast amount of experimental and theoretical effort has been devoted to explore this family of compounds, evidenced by more than 15,000 articles published since 2008 according to the latest reviews, see e.g. Refs.⁴⁻⁷ and references therein. Therefore, in the following we will focus on the previous research work most relevant to provide a proper context for the discussion of the open problem which we have addressed, and the new results on the normal state spectral properties we obtained.

It is generally recognised that the ground state properties of the ferropnictide parent compounds are mostly well described by first principles density functional theory (DFT) calculations, indicating that the low energy excitations are mainly due to electrons in the Fe-3d

orbitals.^{8,9} For LaOFeAs , calculations were carried out almost simultaneously in a number of works.¹⁰⁻¹⁴ The Fermi surface topology and band structure are rather similar for the 11 (e.g. FeSe), 111 (e.g. LiFeAs , NaFeAs), 122 (e.g. BaFe_2As_2 , CaFe_2As_2 , EuFe_2As_2), 1111 (e.g. LaOFeAs , LaFePO , SmFeAsO , CeFeAsO) series of iron-based superconductors.¹⁵⁻¹⁹ However, as a function of doping the agreement between DFT calculations and ARPES experiments in materials like LaOFeAs diminishes,¹² and unexpected Fermi surface topology changes were found as a function of temperature and doping.²⁰⁻²³

Theoretical predictions showed that the 1111 compounds consist of two quasi-2D Fermi cylinders at the zone center (Γ) and a massive 3D hole pocket at the Z-point.^{10,24} This behavior was observed by ARPES and quantum oscillation measurements.²⁵ On the other hand, in the case of 122 compounds, observations related to the dimensionality of the electronic structure revealed quite different behavior, i.e. a more 3D nature of the electronic structure was found in electron doped BaFe_2As_2 ^{26,27} whereas a quasi-2D electronic structure was derived for the case of K-doped BaFe_2As_2 .²⁸ Interestingly, Lui et al.²⁹ showed a transformation of the nature of the electronic structure of CaFe_2As_2 from quasi-2D to more 3D as a function of temperature, going from the high-temperature tetragonal to the low-temperature or-

thorhombic phases.

Many aspects of the temperature dependence of the normal state spectral properties remain largely unstudied in ferropnictides, which motivated our present work. Here, we present our study of the changes with temperature and doping of the normal state electronic structure, throughout the Brillouin zone (BZ). We compare our results with ARPES experimental and previous theoretical results, where feasible, and have been able to predict interesting non-trivial temperature dependent effects at Brillouin zone points, yet unexplored by ARPES. To do this, we employed a minimal microscopic model, which includes two effective bands³⁰ to describe the low energy band structure, as well as intra- and inter-orbital local Coulomb interactions, as detailed in next section. Similar effective two-orbital models have been studied before, focusing on other aspects of the problem, mostly on the superconducting properties. For example, investigations of pairing mechanisms and gap symmetry were reported,^{31–38} studies of spin fluctuations^{31,32,34} and a spin-density wave phase,³⁹ Mott transition for strong electron correlations,^{40–42} lattice and orbital properties,^{42–45} etc. In our case, we studied the minimal microscopic two-orbital model using analytical perturbative techniques to take into account the effect of electron correlations, in order to determine the relevant normal state Green's functions and the corresponding temperature-dependent electronic spectral density. We would like to highlight the fact that, in contrast to other analytical techniques, in our approach a k -dependent self-energy is obtained, also dependent on temperature and doping, enabling us to explore normal state physical properties throughout the Brillouin zone, and thus address new problems.

Our perturbative treatment for the electronic correlations in ferropnictides is justified by previous estimations of intermediate values for them, both from numerical calculations and experimental results. For example, a combination of local density approximation for DFT and dynamical mean field theory (DMFT) calculations for REOFeAs (RE = La, Ce, Pr, and Nd),⁴⁶ estimated a Hubbard local intra-orbital correlation value: $U \sim 3.69$ eV. Refs.^{11,47} estimated that with $U = 4$ eV, width of Fe-bands $W_{Fe} = 3$ eV from LDA, and a Hund's coupling energy $J = 0.7$ eV, taking for the inter-orbital correlation $V = U - 2J$ as in most refs.,^{46,48–53} in this case yielding $V = 2.6$ eV, the available normal state ARPES results could be described, while the same parameters were also adopted for studying the superconducting state in Ref.⁴⁸. Furthermore, it was concluded⁴⁷ that $U = 4.5$ eV would transform the system into a Mott-insulator, in contrast to other LDA+DMFT predictions,^{49–52} reporting that the system remains metallic and does not transform into a Mott-insulator even increasing U up to 5 eV, with $W_{Fe} = 4$ eV and $J = 0.7$ eV; while for $J = 0$ an electronic structure characteristic of much weaker correlations is obtained, with a quasiparticle weight renormalization factor $Z \sim 0.8$.⁵² From ARPES, mass renor-

malization factors between 1.5 and 2.5 were estimated in 122 compounds of the form $Sr_{1-x}K_xFe_2As_2$, depending on the Fermi surface sheet,^{54–57} with similar reports of 1.3 - 2.1 for 1111 and other 122 compounds.^{25,58,59} X-ray absorption spectroscopy estimations of U , placed it below ~ 4 eV.^{60,61} To describe the smaller experimental Fermi-surface areas reported in de Haas-van Alphen experiments in $SrFe_2As_2$,⁵⁸ a renormalization of the LDA band structure was suggested in 2009,⁶² estimating an interband scattering of magnitude ~ 0.46 eV between hole and electron bands to explain the reported experimental band shifts.²⁵ Regarding the minimal two-orbital model by Raghu et al. of Ref.³⁰, the full bandwidth of the non-interacting band structure is about 12 eV, and local intra-orbital correlation values $U/W = 0.2 - 0.5$ have been used previously.^{31,32} Adding Hund's coupling J and local Coulomb correlations, a Mott transition in the two-orbital model³⁰ was predicted at a critical interaction $U_c/W \sim 2.66/(1 + J/U)$,⁴¹ if $J/U < 0.01$, with a decrease of U_c for larger J : deducing that the effect of increasing Hund's coupling on critical U_c is similar to the effect of having more degenerate orbitals in a multi-orbital Hubbard model,⁴¹ effectively weakening the effect of correlations⁵² and stabilizing a metallic state.⁴¹

In addition to effective two-orbital models for ferropnictides, other multi-orbital effective models were proposed.⁴ A three-orbital Hamiltonian was constructed involving the $3d$ orbital xz, yz and xy for Fe⁶³, and compared with the two-orbital model of Ref.³⁰. Improvement of two shortcomings of the latter were reported, related to the relative weights of each orbital on the Fermi surface. Also effective four-orbital⁴¹ and five-orbital models^{4,11,32,48,53,64} were studied. Nevertheless, the effective two-orbital model of Ref.³⁰ is still recognized as a useful minimal model to describe the main features of the low-energy physics of ferropnictides.^{31–37,41,42,66}

Our paper is organized as follows. In Section II A we present the microscopic correlated two-orbital model adopted for our study of the normal state of Fe-based superconductors, and describe the analytical Green's function approach we used to calculate the electronic spectral density function and the total density of states including the correlations in second-order of perturbations (further details of our analytical calculations appear in Supplementary Appendix A). In Section III we present and discuss electronic structure results obtained at different temperature and doping values along the Brillouin zone, and compare them with available theoretical and experimental ARPES results for the normal state spectral properties of ferropnictides. To understand the origin of the non-trivial temperature dependence we predict for the density of states, in Supplementary Appendix B we analyze the k -dependent electron self-energies obtained in our approach, having identified a number of specific Brillouin zone points, not probed by ARPES experiments yet, where we find the largest non-trivial effects of temperature on the renormalization. We conclude in Section IV, summarizing our main findings with the mini-

mal model for pnictides and analytical treatment used, prompting for new ARPES experiments which could test our predictions, and mentioning possible extensions and applications of our work.

II. MICROSCOPIC MODEL AND ANALYTICAL APPROACH.

A. Correlated effective two-orbital model.

To describe analytically the properties of ferropnictides, we will consider a simplified model which contains the minimum number of degrees of freedom preserving the essential physics of the problem in 1111 and 122 compounds, as mentioned in previous section. In particular, a minimal two-orbital model suitable to describe the Fermi surface topology of ferropnictides was proposed by Raghu et al. in Ref.³⁰. The model consists of a two-dimensional square lattice, with each site having two degenerate orbitals. Raghu et al. in Ref.³⁰ fitted the bare-band tight-binding parameters, to obtain an effective band structure which, after folding the Fermi surface to the two Fe/cell Brillouin zone, exhibits two hole pockets around the Γ point and two electron pockets around the M point, which are characteristic of the majority of FeAs compounds.^{15–19} On the large one Fe/cell Brillouin zone, which we will be using in this work, the unfolded Fermi surface includes a hole-related band, relevant to the description of the physics near the Γ point, and an electron-related band to describe the physics near the M point. The two-orbital model was also shown to be suitable to describe the extended s-wave pairing believed to be relevant for ferropnictides, and other details of the superconducting phase.^{31–37,66}

In this work, we will study the doping and temperature effects on the electronic structure and spectral properties, using the following microscopic model for the normal state of pnictides:

$$\mathcal{H} = \mathcal{H}_0 + V_{int}. \quad (1)$$

Thus, we will be modelling these compounds by an effective extended Hubbard model: consisting of two correlated electronic orbitals, described by Hamiltonian \mathcal{H}_0 including the two effective bands proposed by Raghu et al.³⁰ in the large BZ with one Fe atom/unit cell, and local intra- and interorbital electronic correlations included in V_{int} . Concretely:

$$\mathcal{H}_0 = \sum_{k,\sigma} \left[E_c(k) c_{k\sigma}^\dagger c_{k\sigma} + E_d(k) d_{k\sigma}^\dagger d_{k\sigma} \right] \quad (2)$$

where the operators $c_{k\sigma}^\dagger$ and $d_{k\sigma}^\dagger$ create an electron in the respective c and d effective bands, with spin $\sigma = \uparrow, \downarrow$ and crystal momentum \vec{k} while, following Ref.³⁰, we consider for the two bare effective bands:

$$E_{c,d}(\vec{k}) = \epsilon_+(\vec{k}) \pm \sqrt{\epsilon_-^2(\vec{k}) + \epsilon_{xy}^2(\vec{k})} - \mu \quad (3)$$

μ denotes the chemical potential: notice that we refer the energies to μ , since we will adopt the grand canonical ensemble in our Green's function treatment of the system, like in Ref.³⁰. σ denotes the spin degrees of freedom, and

$$\epsilon_\pm(\vec{k}) = \frac{\epsilon_x(\vec{k}) \pm \epsilon_y(\vec{k})}{2} \quad (4)$$

$$\epsilon_{xy}(\vec{k}) = -4t_4 \sin(k_x) \sin(k_y)$$

$$\epsilon_x(\vec{k}) = -2t_1 \cos(k_x) - 2t_2 \cos(k_y) - 4t_3 \cos(k_x) \cos(k_y)$$

$$\epsilon_y(\vec{k}) = -2t_2 \cos(k_x) - 2t_1 \cos(k_y) - 4t_3 \cos(k_x) \cos(k_y)$$

where the parameters $t_i, i = 1, 4$, denote the hopping amplitudes between sites on the square lattice formed by the Fe atoms³⁰ in ferropnictides.

As for the electronic correlations, we assume that short-range Hubbard-like electron-electron interactions are present, and consider two local correlations between the effective orbitals at each site (as in Refs.^{30,31}): intra-orbital Coulomb repulsion U , and inter-orbital repulsion V . Therefore V_{int} has the following form:

$$V_{int} = \sum_i [U (n_{i\uparrow} n_{i\downarrow} + N_{i\uparrow} N_{i\downarrow}) + V (n_{i\uparrow} + n_{i\downarrow}) (N_{i\uparrow} + N_{i\downarrow})] \quad (5)$$

Here: $n_{i\sigma} = c_{i\sigma}^\dagger c_{i\sigma}$ and $N_{i\sigma} = d_{i\sigma}^\dagger d_{i\sigma}$, and i denotes the lattice sites. Fourier transforming, V_{int} can be written in k -space as follows:

$$\begin{aligned} V_{int} = & \frac{U}{N} \sum_{k_1, k_2, k_3} \left[c_{k_1\uparrow}^\dagger c_{k_2\uparrow} c_{k_3\downarrow}^\dagger c_{k_1-k_2+k_3\downarrow} + d_{k_1\uparrow}^\dagger d_{k_2\uparrow} d_{k_3\downarrow}^\dagger d_{k_1-k_2+k_3\downarrow} \right] \\ & + \frac{V}{N} \sum_{k_1, k_2, k_3} \left[c_{k_1\uparrow}^\dagger c_{k_2\uparrow} d_{k_3\uparrow}^\dagger d_{k_1-k_2+k_3\uparrow} + c_{k_1\uparrow}^\dagger c_{k_2\uparrow} d_{k_3\downarrow}^\dagger d_{k_1-k_2+k_3\downarrow} \right] \\ & + \frac{V}{N} \sum_{k_1, k_2, k_3} \left[c_{k_1\downarrow}^\dagger c_{k_2\downarrow} d_{k_3\uparrow}^\dagger d_{k_1-k_2+k_3\uparrow} + c_{k_1\downarrow}^\dagger c_{k_2\downarrow} d_{k_3\downarrow}^\dagger d_{k_1-k_2+k_3\downarrow} \right] \end{aligned} \quad (6)$$

B. Our electronic structure calculation for ferropnictides.

The total electron spectral density to be compared with ARPES experiments is $A(\vec{k}, \omega)$, which in our effective extended Hubbard model is defined by:

$$A(\vec{k}, \omega) = A_c(\vec{k}, \omega) + A_d(\vec{k}, \omega) \quad (7)$$

with contributions from both electron bands given by:

$$A_{c\sigma}(\vec{k}, \omega) = -\frac{1}{\pi} \text{Im} G_{\sigma}^{\text{ret}}(k, \omega); \quad A_{d\sigma}(\vec{k}, \omega) = -\frac{1}{\pi} \text{Im} F_{\sigma}^{\text{ret}}(k, \omega) \quad (8)$$

Here: $G_{\sigma}^{\text{ret}}(k, \omega)$ and $F_{\sigma}^{\text{ret}}(k, \omega)$ denote the retarded Green's functions corresponding to the c and d electrons in our two effective bands, i.e.

$$G_{\sigma}^{\text{ret}}(\vec{k}, \omega) = G(k, \omega + i\delta) = \ll c_{k\sigma}; c_{k\sigma}^{\dagger} \gg (\omega + i\delta) \quad (9)$$

$$F_{\sigma}^{\text{ret}}(\vec{k}, \omega) = F(k, \omega + i\delta) = \ll d_{k\sigma}; d_{k\sigma}^{\dagger} \gg (\omega + i\delta) \quad (10)$$

where δ is an infinitesimal positive number. Integrating the spectral density over the 1st Brillouin zone, yields the total density of states (TDOS), or local spectral function:

$$A(\omega) = \sum_{k \in BZ} A(k, \omega) \quad (11)$$

We calculated the temperature-dependent Green's functions using Zubarev's equations of motion (EOM) formalism,^{67,68} i.e.:

$$\omega \ll \hat{A}; \hat{B} \gg = \frac{1}{2\pi} \langle \{ \hat{A}, \hat{B} \} \rangle + \ll [\hat{A}, \hat{H}]; \hat{B} \gg (\omega)$$

where \hat{A} and \hat{B} are fermionic operators, $\ll \hat{A}; \hat{B} \gg$ is the time Fourier-transform of the retarded Green's function $-i\theta(t-t') \langle \hat{A}(t) \hat{B}(t') + \hat{B}(t') \hat{A}(t) \rangle$, where the time-dependent operators appear in Heisenberg representation, and the expectation value is calculated using the appropriate statistical ensemble at finite temperature T (or the ground state of the system, at $T=0$)⁶⁷. In our case, we study the normal state of the system at temperature T , and in particular evaluate the required expectation values in the paramagnetic normal phase, using the grand canonical ensemble.

We obtained the following exact coupled set of equations of motion for $G_{\sigma}(k, \omega)$ and $F_{\sigma}(k, \omega)$, respectively:

$$\begin{aligned} [\omega - E_c(k)] G_{\sigma}(k, \omega) &= \frac{1}{2\pi} + \sum_{k_1, k_2} \left[\frac{U}{N} \Gamma_1(k_1, k_2, k, \omega) \right. \\ &\left. + \frac{V}{N} \Gamma_2(k_1, k_2, k, \omega) + \frac{V}{N} \Gamma_3(k_1, k_2, k, \omega) \right] \quad (12) \end{aligned}$$

$$\begin{aligned} [\omega - E_d(k)] F_{\sigma}(k, \omega) &= \frac{1}{2\pi} + \sum_{k_1, k_2} \left[\frac{U}{N} \Gamma_4(k_1, k_2, k, \omega) \right. \\ &\left. + \frac{V}{N} \Gamma_5(k_1, k_2, k, \omega) + \frac{V}{N} \Gamma_6(k_1, k_2, k, \omega) \right] \quad (13) \end{aligned}$$

where in Eq. 12 we denoted:

$$\begin{aligned} \Gamma_1(k_1, k_2, k, \omega) &\equiv \Gamma_{\sigma, \bar{\sigma}, \bar{\sigma}}^{\text{ccc}}(k_1, k_2, k, \omega) = \\ &= \ll c_{k_2, \sigma} c_{k_1, \bar{\sigma}}^{\dagger} c_{k_1 - k_2 + k, \bar{\sigma}}; c_{k\sigma}^{\dagger} \gg (\omega) \\ \Gamma_2(k_1, k_2, k, \omega) &\equiv \Gamma_{\sigma, \sigma, \sigma}^{\text{cdd}}(k_1, k_2, k, \omega) \\ \Gamma_3(k_1, k_2, k, \omega) &\equiv \Gamma_{\sigma, \bar{\sigma}, \bar{\sigma}}^{\text{cdd}}(k_1, k_2, k, \omega) \quad (14) \end{aligned}$$

and in Eq. 13:

$$\begin{aligned} \Gamma_4(k_1, k_2, k, \omega) &\equiv \Gamma_{\sigma, \bar{\sigma}, \bar{\sigma}}^{\text{ddd}}(k_1, k_2, k, \omega) \\ \Gamma_5(k_1, k_2, k, \omega) &\equiv \Gamma_{\sigma, \sigma, \sigma}^{\text{dcc}}(k_1, k_2, k, \omega) \\ \Gamma_6(k_1, k_2, k, \omega) &\equiv \Gamma_{\sigma, \bar{\sigma}, \bar{\sigma}}^{\text{dcc}}(k_1, k_2, k, \omega) \quad (15) \end{aligned}$$

having introduced the following notation, above, for simplicity:

$$\Gamma_{\sigma_{\alpha} \sigma_{\beta} \sigma_{\gamma}}^{\alpha, \beta, \gamma}(k_1, k_2, k, \omega) \equiv \ll c_{\alpha k_2, \sigma_{\alpha}} c_{\beta k_1, \sigma_{\beta}}^{\dagger} c_{\gamma k_1 - k_2 + k, \sigma_{\gamma}}; c_{k\sigma}^{\dagger} \gg (\omega) \quad (16)$$

where $c_{\alpha}, c_{\beta}, c_{\gamma}$ describe c- or d-annihilation operators and $\sigma_{\alpha}, \sigma_{\beta}, \sigma_{\gamma}$ their spins (σ , or $\bar{\sigma}$), as required by each equation (more details in supplementary Appendix A).

Notice that the Hartree-Fock solution to this problem would be obtained by closing this set of equations of motion in first-order, with a mean-field approximation of Γ_i ($i = 1, 6$) in terms of $G_{\sigma}(k, \omega)$ and $F_{\sigma}(k, \omega)$, as detailed in supplementary Appendix A.

In our work, instead, we calculated the equations of motion for the three Γ_i ($i = 1, 3$) functions coupled to $G(\vec{k}, \omega)$ in first order as stated in the previous equations; and proceeded likewise for Γ_i ($i = 4, 6$) coupled to $F(\vec{k}, \omega)$. Each of these second-order equations of motion introduces three new coupled higher-order Green's functions in the problem.

To close and solve the coupled set of equations of motion in second-order, we used the following approximation: all higher-order Green's functions introduced in each subset of equations of motion for Γ_i ($i = 1, 3$), were approximated in mean-field in terms of Γ_i ($i = 1, 3$) and $G(\vec{k}, \omega)$ (introducing proper average values), yielding a 4×4 closed set of equations of motion (for details, see supplementary Appendix A). We proceeded likewise for the subset of equations for Γ_i ($i = 4, 6$) related to $F(\vec{k}, \omega)$. Notice that this RPA-like approximation leads to a second-order closed system of eqs. of motion for $G, \Gamma_1, \Gamma_2, \Gamma_3$; and an analogous one for $F, \Gamma_4, \Gamma_5, \Gamma_6$; which after lengthy calculations we could solve. In supplementary Appendix A we detail the full expressions obtained for these Green's functions, which might be used to calculate other normal state properties, and in supplementary Appendix B we discuss the corresponding k-dependent electron self-energies, which are obtained in our level of approximation.

The decoupling scheme proposed for the higher order Green's functions, which appear coupled in the EOM, accounts for the self-energy effects of the single-particle Green's function. These self-energy effects may describe both intra- and inter-orbital coupling with equal and opposite spins at lowest order (charge and spin fluctuations), thus leading to band splitting effects, which are not a mere renormalization of the energy spectrum. This fact is well known for other Hubbard-like models (see e.g. Refs.^{68,69}), and the band splitting effects may lead to a metal-insulator transition or to charge and spin instabilities.

We shall be interested in describing the behavior of this many-particle system at finite temperatures. For a system in thermodynamic equilibrium the expectation value of any operator may be computed by using the grand-canonical ensemble. To complete our solution in RPA approximation, the total electron band filling n (or the chemical potential μ) at temperature T is determined self-consistently by the following equation:

$$n(\mu) = \int \frac{d\vec{k}}{(2\pi)^2} \frac{d\omega}{2\pi} \left[A_c(\vec{k}, \omega) \frac{1}{e^{\beta E_c(\vec{k})} + 1} + A_d(\vec{k}, \omega) \frac{1}{e^{\beta E_d(\vec{k})} + 1} \right] \quad (17)$$

Thus, a major self-consistent set of coupled equations has to be solved, since the total spectral density function, which we obtain by solving two coupled sets of Green's functions, is required and will be integrated over the Brillouin zone (\vec{k}) and all energies ω , weighed by the Fermi occupation factors of each effective band at temperature T . The thermodynamic state of the system is defined by the parameter μ and β , the inverse temperature measured in energy units, i.e. $\beta = \frac{1}{k_B T}$, where k_B is Boltzmann's constant. Zero temperature, or $\beta \rightarrow \infty$, describes the ground state of the system. Notice that in this model, half-filling ($n = 2$) corresponds to the ferro-pnictide parent compounds.

As detailed in supplementary Appendix A, to evaluate the Green's functions $G_\sigma(k, \omega)$ and $F_\sigma(k, \omega)$, we need to perform double and triple summations over the first Brillouin zone of the crystal lattice. For simplicity, we have assumed a square lattice, as done previously,³⁰ and have performed the BZ summations using the Chadi-Cohen BZ sampling method.⁷⁰

III. RESULTS AND DISCUSSION

Below, we present electronic structure results at different temperature and doping values, which we obtained for the normal state of ferro-pnictides with the extended Hubbard model and our analytical treatment presented in previous section, and compare them with available theoretical and experimental ARPES results in ferro-pnictides. The self-consistent sets of equations obtained for the Green's functions detailed in previous section, were solved numerically using the following tight-binding interaction parameters: $t_1 = -1$ eV, $t_2 = 1.3$ eV, $t_3 = t_4 = -0.85$ eV, adopted in Ref.³⁰ for the two effective bands in the large one Fe/cell Brillouin zone: BZ which was also used throughout our work. In the figure captions we specify the precision used in the Chadi-Cohen sampling method⁷⁰ for Brillouin zone summations, including the order ν used. We found good convergence in most results using the seventh order ($\nu = 7$) of the Chadi-Cohen method,⁷⁰ but the spectral function and total density of states results here presented were obtained using ninth or eighth order, respectively, for improved accuracy. Note that $\nu = 8$ -th order for the square-lattice BZ sampling

implies using 8,256 special BZ points, while $\nu = 9$ implies using 32,896 ones.⁷⁰

We will start by analyzing in subsection III A the effect of correlations in our model, comparing our calculations of the density of states to previous known results, like experimental data now available for 1111 and 122 compounds, in order to obtain a qualitative estimation of the relevant magnitudes of U and V in the model.

Next, in subsection III B we exhibit the momentum dependence of the spectral density function along symmetry paths of the square lattice Brillouin zone (BZ), comparing our results with reported ARPES data. Notice that in order to allow for direct comparison with the published ARPES intensity results, the same treatment is adopted here for the data: i.e. all spectral density data here presented (denoted $\tilde{A}(\vec{k}, \omega)$, here) have been convoluted with an energy resolution of 30 meV, and also multiplied by the Fermi-Dirac function $f_{FD}(\omega)$ at temperature T as in the experimental references cited.

Subsequently, in subsection III C we study the effects of hole and of electron doping in terms of our model, and compare them with the electronic properties of ferro-pnictides observed in ARPES. Finally, in subsection III D we study and compare with available experimental data the temperature dependence of the total density of states and the spectral density at the most relevant BZ points.

A. Effect of intra- and inter-orbital Coulomb interactions on the total density of states $A(\omega)$

As discussed in the Introduction, previous theoretical and experimental research works estimate intermediate values for the electronic correlations, i.e. most of them placing the local intra-orbital Hubbard repulsion in the range $U \sim 3.69$ eV for ReFeAsO (Re= Ce, Pr, Nd)⁴⁶ to $U = 4.5$ eV for LaO_{1-x}F_xFeAs,^{47,52} while X-ray absorption experiments suggest $U \leq 4$ eV for LaO_{1-x}F_xFeAs,⁶¹ and BaFe₂As₂.⁶⁰ For the inter-orbital correlation V similar values are estimated in calculations for Fe-Se compounds.⁵³

We analyzed the separate effects of the intra- and inter-orbital correlation parameters included in the model. First, the total density of states $A(\omega)$, is shown in Fig. 1(a). for different values of intra-orbital U and a fixed inter-orbital: $V = 3.5$ eV, at half-filling $n = 2$ and temperature $T = 20$ K. We find a large spectral weight reduction at the Fermi level in the range $U = 3.7 - 3.9$ eV, with an important spectral weight redistribution around the Fermi level.

In Fig. 1(b), we focus on the effect of the inter-orbital Coulomb interaction V on the density of states. Note that the TDOS is almost independent of V , in the range of U values analyzed. We thus confirm that the most relevant Coulomb correlation in 1111 and 122 systems is in fact the local intra-orbital repulsion U , in agreement with previous research work.^{7,37}

In the following, we will focus on the dependence of the

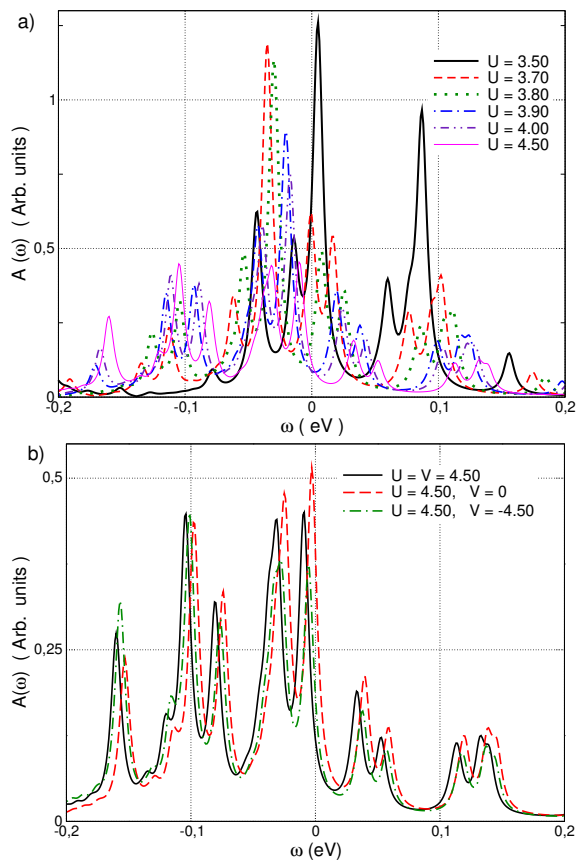


FIG. 1. a) Dependence of total DOS $A(\omega)$ on the intra-orbital repulsion U , for fixed $V = 3.5\text{eV}$; b) Effect of the inter-orbital local Coulomb interaction V on the total DOS, for fixed $U = 4.5\text{eV}$. At half-filling: $n = 2$, and temperature: $T = 20\text{K}$; and as in Ref.³⁰: $t_1 = -1.0$, $t_2 = 1.3$, $t_3 = t_4 = -0.85$ (in eV). Chadi-Cohen BZ summations order: $\nu = 8$. Note that ω is measured w.r. to μ , in our treatment. All energies are given in eV, henceforth.

electronic structure on crystal momentum, doping and temperature, fixing the local Coulomb interactions as: $U = V \sim 3.50\text{eV}$, typical intermediate correlation values characteristic of Fe-pnictide compounds as previously discussed.^{52,60,61,71} Being the total bandwidth $W \sim 12\text{eV}$ for the non-interacting effective band structure of Ref.³⁰, the value $U = 3.5\text{eV}$ corresponds approximately to $0.29W$.

B. Momentum dependence of the spectral density $\tilde{A}(\vec{k}, \omega)$

Our analysis of the two-orbital extended Hubbard model included the calculation of the one-particle spectral function. In this section, we will show our electronic structure results along two BZ paths, namely along $\Gamma - X$ in Fig. 2(a), and along $\Gamma - M$ in Fig. 2(b), where: $\Gamma = (0, 0)$, $X = (\pi, 0)$ and $M = (\pi, \pi)$. These paths were

chosen as they allow us to compare our results with available ARPES data, in particular those of Refs.^{65,72-74}. Concretely, we here show the evolution of the spectral function $A(\vec{k}, \omega)$ as a function of momentum \vec{k} , at low temperature: $T = 20\text{K}$, and at half-filling: $n = 2$ (i.e. for the parent compounds).

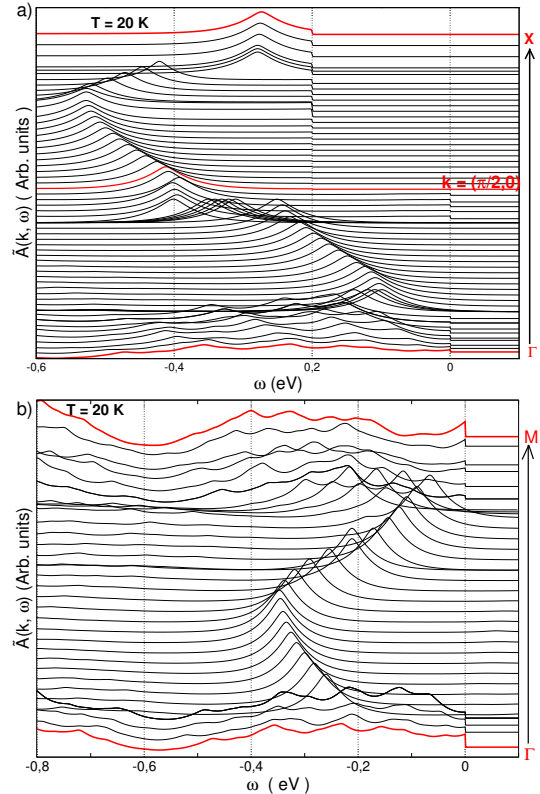


FIG. 2. a) Spectral density $\tilde{A}(\vec{k}, \omega)$ (i.e. convoluted with an exp. resolution of 30meV , and multiplied by $f_{FD}(\omega)$, as in expts.) as a function of energy ω , for different BZ points (shown vertically displaced) along the symmetry path from Γ (bottom curve) to X (top curve). b) $\tilde{A}(\vec{k}, \omega)$ as a function of ω , for different BZ points along $\Gamma - M$. At $T = 20\text{K}$, and $n = 2$ (as in Ref.⁶⁵). Here: $U = V = 3.5\text{eV}$; $\mu = 0.15\text{eV}$. Chadi-Cohen BZ summations order: $\nu = 9$. Other parameters as in Fig. 1.

In particular, in Fig. 2(a) notice that a relatively flat multiple-peak structure near Γ , evolves into a sharp peak near the Fermi level at X . In accordance with ARPES experiments along $\Gamma - X$, e.g. in $\text{LaOFe}(\text{P}, \text{As})$, (Fig. 4 of Ref.⁶⁵) in $\text{K}_x\text{Fe}_{2-y}\text{Se}_2$ (Fig. 2 of Ref.⁷³) and $\text{BaFe}_{1.7}\text{Co}_{0.3}\text{As}_2$ compounds, (Fig. 2 of Ref.⁷⁴) during this evolution, the main peak describes an S-like trajectory including an intermediate regime with a two peak-like structure, though in experiments the width and intensity of these features are material-dependent.

Along $\Gamma - M$, in Fig. 2(b) notice how the broad relatively flat structure near Γ and near M , for intermediate BZ points develops a peak-like structure which describes a trajectory similar to that reported in ARPES

experiments: (concretely, Fig. 1 of Ref.⁷⁴ and Fig. 1 of Ref.¹⁵) in particular, it resembles the evolution of the ARPES peak in LaFeAsO assigned to two bulk-related energy bands in Ref.¹⁵, where a second peak-like structure closer to the Fermi level but related to surface-bands is also shown. Very recently, ARPES in FeSe single crystals reported⁷⁵ very similar energy distribution curves along $\Gamma - M$ in their Figures 1 and 2.

Notice that the spectral density results shown in Figs. 2(a) and 2(b) include renormalization effects due to the correlations which are taken into account by our analytical approach, concretely by the electron self-energies obtained, discussed in Supplementary Appendix B, which depend explicitly on crystal momentum k , as well as temperature and doping. Band renormalization effects such as these, implying changes to the non-interacting electron band structure of the minimal model proposed in Ref.³⁰ (in particular, to their Fig. 2(a)), have also been reported in several ARPES experiments: e.g. in Refs.^{20,54,74}.

C. Effect of doping on the electronic structure

We will now refer to the effects of doping on the total density of states, and in particular the degree of accuracy presented by the results obtained with our approach, taking advantage of the experimental data available for comparison, such as Refs.^{76,77}. In Supplementary Appendix C we complement these results, showing also the effects of doping on the spectral density function at the Γ and M symmetry points. We carried out a systematic study covering a broad range of hole and electron doping values, which respectively correspond to less or more electrons in the system than present at half-filling ($n = 2$), which represents the parent compound. In our calculations we fixed the band filling n , while the chemical potential μ was obtained self-consistently according to Eq. 17.

In Fig.3 (a) we exhibit a comparison of the effect of hole vs. electron doping on the renormalized total density of states. In agreement with ARPES experiments in Ref.⁷⁶ (in particular, their Fig. 2(e)), we find that upon increasing hole-doping a rigid-band-like shift of all peaks towards the Fermi level ensues, thus increasing spectral weight there (for more details, see Suppl.Appendix C. In particular, in Figs. C.5 and C.6 the spectral density results at M are shown, and their comparison with experiments is discussed in detail). Meanwhile, when the system is doped with electrons, $n = 2.12$ and $n = 2.25$ in the figure, the bottom of the electronic structure is seen to be shifted to lower binding energies. Notice that for higher electron-doping values, e.g. $n = 2.25$, a sharp intense peak appears at the Fermi level.

For comparison with the results of Figure 3 of Ref.⁷⁶, in our Fig 3 (b) we plot the chemical potential shift: $\delta\mu = \mu(n) - \mu(n = 2)$ with respect to the undoped compound obtained in our approach as a function of the carrier (dopant) density: $\delta n = n - 2$. As indicated in Ref.⁷⁶, experimental chemical potential shifts,

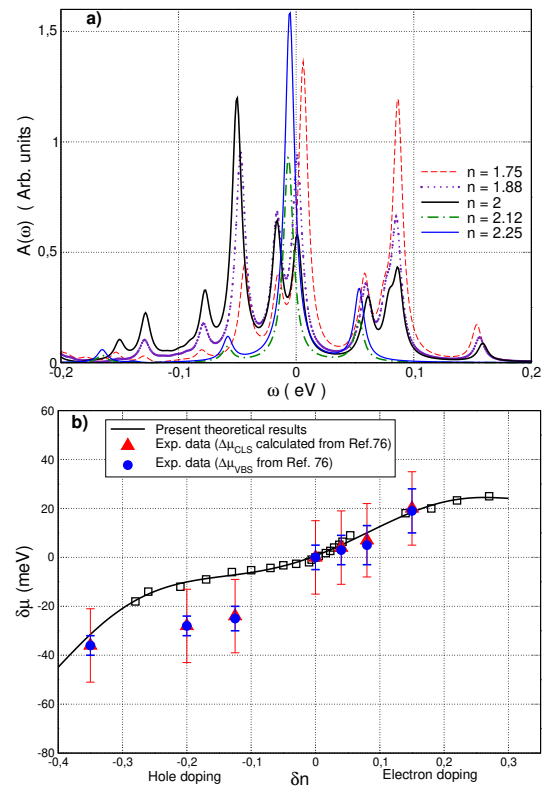


FIG. 3. Electron vs. hole doping. a) Effect on the total DOS. b) Chemical potential shift as a function of carrier (dopant) density, with respect to the parent compound. For the exp. values shown, obtained from reported⁷⁶ core-level shift data $\Delta\mu_{CLS}$ (solid triangles) and valence-band shifts $\Delta\mu_{VBS}$ (solid circles), the carrier density is given as $x/2$ (per Fe): either for $\text{BaFe}_{2-x}\text{Co}_x\text{As}_2$ or $\text{Ba}_{1-x}\text{K}_x\text{Fe}_2\text{As}_2$, respectively for electron or hole doping. At $T = 20$ K, $U = V = 3.5\text{eV}$. Other parameters as in Fig. 1.

which we denote $\Delta\mu_{CLS}$, can be obtained from the doping dependence of the measured As-3d core level shifts (ΔE_{CLS}) reported in their Fig.3.b: by using the formula $\Delta\mu_{CLS} = -\Delta E_{CLS} + (\Delta V_M + \Delta E_R)$, where $(\Delta V_M + \Delta E_R)$ accounts for doping-related changes in the Madelung potential and in the core-carrier screening, respectively, assuming that changes of As-valency upon doping are negligible. Using the As-3d core level shifts and the differences $(\Delta V_M + \Delta E_R)$ reported in Fig.3(b) of Ref.⁷⁶, we calculated the experimental chemical potential shifts derived from core-level shift data $\Delta\mu_{CLS}$ corresponding to the seven compounds experimentally studied, and have plotted them in our Figure 3(b). A comparison with the theoretical results of our approach, shows that the asymmetry and especially the different signs exhibited by the chemical potential shifts for hole and electron doping are described, in agreement with experiments.^{25,76} Notice that our theoretical results also describe the correct monotonous dependence of the chemical potential shift as a function of doping for all samples, and quantitative agreement is also obtained within the

experimental error bars of $\Delta\mu_{CLS}$ for all the electron-doped samples as well as for the sample with the highest hole-doping. For completeness, in Figure 3(b) we also include the experimental chemical shifts, denoted by $\Delta\mu_{VBS}$, obtained as $\Delta\mu_{VBS} = -\Delta E_{VBS}$ from the valence-band shift data (ΔE_{VBS}) reported in Fig.3(c) of Ref.⁷⁶, which are consistent with $\Delta\mu_{CLS}$ obtained from the measured As-3d core level shifts. The reported electron-hole asymmetry in Ba-122 pnictides,⁷⁶ in particular in BaFe₂As₂, has been also observed in the superconducting phase.^{20,76,79,80} We checked that the chemical potential shift is almost independent of V , consistently with our DOS results discussed in Section III A.

Let us first stress one result: notice that in spite of the band renormalization effects due to correlations known to be included in our level of approximation (as shown in our self-energy analysis of Suppl.Appendix B), we obtain electron-hole asymmetric effects such as experimentally observed^{76,77} i.e. the bottom of the band is shifted to lower, or higher, binding energies with respect to the Fermi level upon, respectively, electron or hole doping, as one would expect if the electronic structure is not changed by doping.

Next, we would like to stress that, even though one might expect the values of the chemical potential shifts upon doping to be material-dependent, we find that our results in Fig.3(b) agree better with the reported data on Ba-122 compounds (Figure 3 of Ref.⁷⁶) than the LDA calculations mentioned in Ref.⁷⁶: which required dividing their calculated chemical potential shift values by a factor of 4, in order to achieve quantitative agreement with experiments. Previously, theoretical estimations⁶² of an LDA band structure renormalization, amounting to a factor of 2 division, had been indicated as necessary to describe with LDA the observed energy shifts of the electron and hole bands.²⁵

Thus, our analytical treatment for the effective two-band model yields electronic structure results describing not only the observed opposite chemical potential shifts for electron and hole-doping, but the chemical potential shift values we obtain are in quantitative agreement with the experimental results of Fig. 3 of Ref.⁷⁶, respectively for all electron doped samples in BaFe_{2-x}Co_xAs₂ and for the sample with highest hole doping in Ba_{1-x}K_xFe₂As₂.

As mentioned in the Introduction, Lifshitz transitions have been reported for ferropnictides, in particular as a function of doping.^{20,22,23} We have checked that the correlated two-orbital model indeed undergoes changes of topology of the Fermi surface upon doping increase, as exhibited in Figure C.8 of Suppl. Appendix C. A detailed study of this topic is out of the scope of the present work, though we plan to address it in the future.

D. Effects of temperature on the spectral properties

Our analytical approach is specifically well adapted to shed light on the temperature dependence of the normal state spectral properties throughout the Brillouin zone, subject largely unstudied in ferropnictides, on which we were able to find interesting predictions.

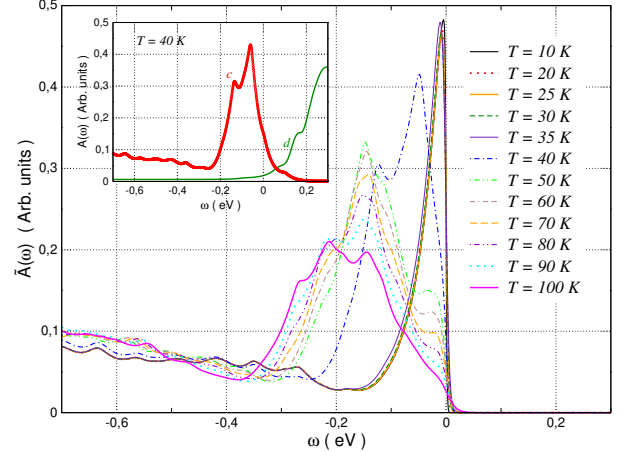


FIG. 4. Temperature dependence of $\tilde{A}(\omega)$. Parameters: $U = V = 3.5$ eV, $n = 2$. Other parameters as in Fig. 1. Inset: partial c- and d-band densities of states at 40 K.

First, we will focus on the effect of the temperature on the total density of states. We found only low temperature density of states ARPES data reported for the parent compounds, e.g in Refs.^{65,82}, to compare the results of this section, while at room temperature we only found a hard X-ray photoemission DOS result reported for undoped Ba-122.⁸¹ To allow a direct comparison with experimental data, in this section all density of states results exhibited, denoted $\tilde{A}(\omega)$, have been convoluted with an energy resolution of 30 meV and multiplied by $f_{FD}(\omega)$, as in experiments.^{65,81,82}

In Figure 4 we show the total DOS we obtain for several temperatures varying from 10 K to 100 K. As an inset, we plotted the corresponding partial densities of states at $T = 40$ K, corresponding to the two effective TB bands³⁰ used in our model, denoted by c and d and defined in Eq. 8.

In Fig. 4, notice that with our simplified correlated model for pnictides the total DOS near the Fermi level consists of a sharp intense peak, which the inset and our self-energy results presented in Supplementary Appendix B.1 show is mostly due to the renormalized c-effective band, i.e. obtained in our approach by renormalization of the non-interacting c-band from Eq. 3 proposed by Raghu et al.³⁰, which is the lowest energy effective band extending from -8 to 4 eV. Our result agrees with previous work, which indicates that the peak originates mainly from Fe-3d states, in particular: ARPES experiments at low temperature in

LaOFeP and LaOFeAs compounds (Figure 1 of Ref.⁶⁵) at $T = 20$ K interpreted with DFT+LDA calculations, ARPES at $T = 28.7$ K in FeSe_{1-x} (Figure 2 of Ref.⁸²), and hard X-ray photoemission experiments in BaFe₂As₂ (Figure 2 of Ref.⁸¹) at 20K and 300K. The low temperature results agree also with LDA+DFMT calculations in SmO_{1-x}F_xFeAs,¹¹ LDA+DFT calculations in LaFeAsO_{1-x}F_x,¹⁰ BaFe₂As₂¹³ and LiFeAs.¹³

Regarding the evolution with temperature shown in Fig. 4, our calculations predict that this intense sharp peak near the Fermi level should be clearly observed for temperatures $T < 40$ K. By increasing temperature, we find that the peak near the Fermi level is shifted towards lower binding energy, diminishes intensity and becomes broader, eventually developing additional structure. This agrees with the observations in BaFe₂As₂ (Figure 2 of⁸¹) where, from the sharp peak near the Fermi level at 20 K, at room-temperature a broad hump located at lower binding energies was reported.

Notice in Fig. 4 that we also find new temperature dependent peaks in the DOS due to correlation effects, as our self-energy analysis in Supplementary Appendix B confirms. Concretely, if one compares the density of states curves corresponding to various temperatures in Fig. 4: at 10 K the DOS is dominated by a single peak near the Fermi level, at 40 K we obtain two prominent peaks, shifted further below the Fermi level w.r. the $T=10$ K result, and three sizeable peaks of the density of states (shifted still further below the Fermi level) are present at $T=100$ K. Therefore, we are predicting a non-trivial temperature dependence of the total density of states due to correlations, which it would be interesting to investigate experimentally.

Furthermore, in connection with the location of the peak near the Fermi level, which may be material-dependent: in Fig. 4 we find it centered at $\omega \sim -10$ meV at 30 K, which is similar to the peak position estimated from fits in Ref.⁸² in FeSe_{1-x}, placing it at $\omega = -15$ meV at 30 K, in particular their Figure 2(d).

Next, we will analyze the evolution with temperature of the spectral density, analyzing the changes in $\tilde{A}(\vec{k}, \omega)$. In first term, we will fix \vec{k} at the relevant high-symmetry points of the BZ which have been studied in ARPES experiments.^{15,29}

In Figure 5(a), we show the evolution of the electronic structure with temperature at Γ . Notice that a number of prominent peaks emerge as temperature decreases. This is qualitatively what was observed in ARPES experiments in LaFeAsO (Figure 7(a) of Ref.¹⁵) and CeFeAsO (Figure 4 of Ref.⁷²) compounds, where three peaks were also reported in the same energy range, though our results differ in the relative intensities. Our results also agree qualitatively with recent ARPES experiments at Γ closer to the Fermi level in NaFe_{0.95}Co_{0.05}As (Figure 3(a) of Ref.⁸³) and Ca_{1-x}Na_xFe₂As₂ (Figure 2 of Ref.⁸⁴) compounds, who focus on the spectral density reduction at the Fermi level upon temperature increase.

In Figure 5(b) we show the temperature evolution of

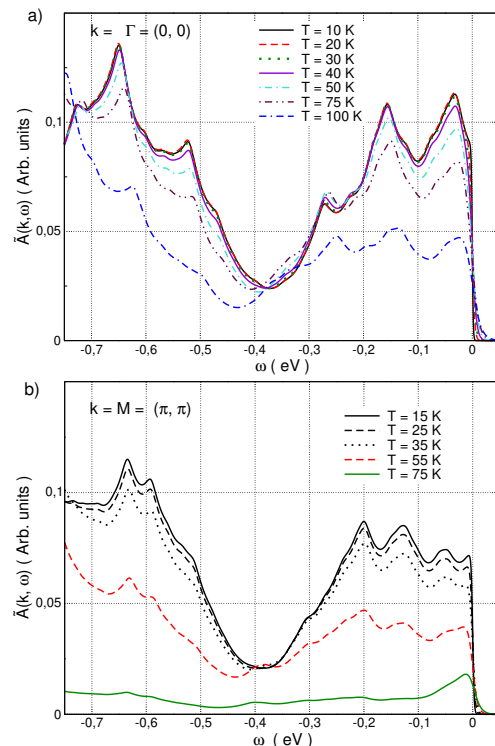


FIG. 5. a) Temperature dependence of $\tilde{A}(k, \omega)$, at Γ ; b) Temperature dependence of $\tilde{A}(k, \omega)$, at M . Same energy range used for the ARPES data of Ref.¹⁵. Parameters: $U = V = 3.5$, $n = 2$, $\nu = 9$. Other parameters as in Fig. 1.

the spectral density at M , to be compared with the reported ARPES data in Figure 3 of Ref.⁷² and Figure 4(b) of Ref.⁸⁵, who focus on the energy range $[-0.2, 0]$ eV. The description of the low temperature ARPES data at M with the effective two-orbital model is not as good as for Γ . Though the spectra at M in the energy range $[-0.1, 0]$ eV exhibit a two-peak structure at low temperature which evolves to a broad single peak at higher temperature, in agreement with ARPES experiments in CeFeAsO (Figure 3 of Ref.⁷²) and EuFe₂As₂ (Figure 4(b) of Ref.⁸⁵) compounds, we find differences (e.g. a number of additional peaks at low temperature below -0.1 eV) if we compare our results with experiments in a wider energy range. The temperature evolution of the electronic structure at Γ exhibits less relevant changes than at M , in agreement with experiments.

In any case, the spectral function results at the high symmetry BZ points probed by ARPES, which are presented in Figs. 5(a) and 5(b), mainly exhibit the usual effects of thermal broadening, in correspondence with the negligible temperature-dependence of the self-energy at these points, discussed in Supplementary Appendix B.

Nevertheless, as discussed in connection with Fig. 4, our model predicts a non-trivial temperature-dependence of the total density of states, to which the whole BZ contributes. To understand this fact, we explored through-

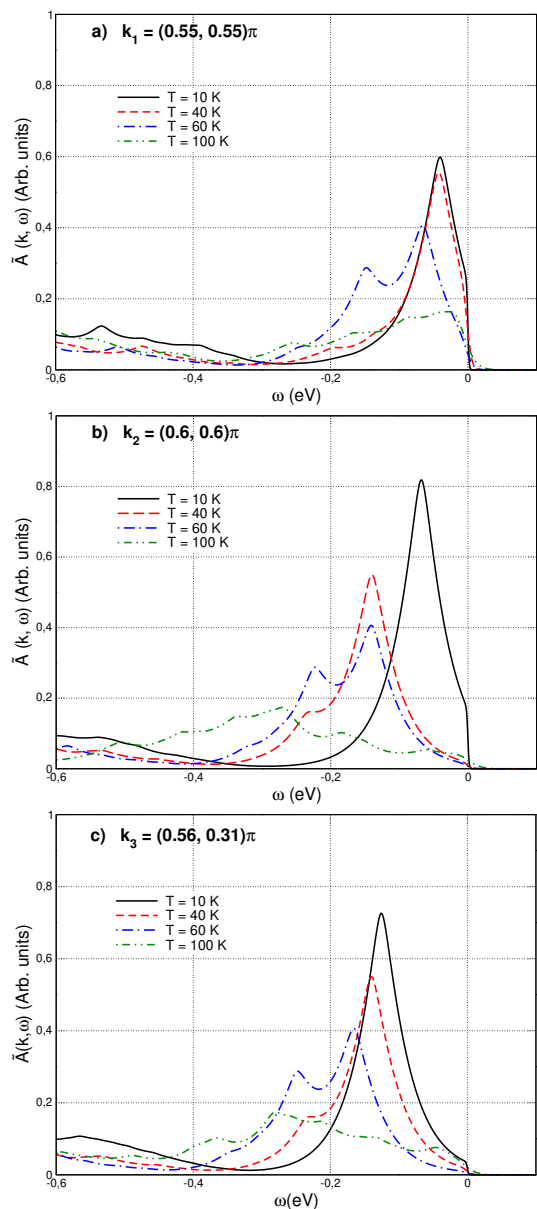


FIG. 6. Temperature dependence of $\tilde{A}(k, \omega)$, at the BZ points respectively indicated in each plot. Parameters: $U = V = 3.5$ eV, $n_c = 1.45$ and $n_d = 0.55$ ($n = 2$), $\nu = 9$. Other parameters as in Fig. 1.

out the whole BZ the dependence on temperature of the k -dependent self-energy obtained in our approach, and in Supplementary Appendix B exhibit our results. Interestingly, for the parent compounds ($n = 2$) we have been able to identify a number of specific BZ points, not yet probed by ARPES, which exhibit sizeable and non-trivial temperature dependent renormalization effects, allowing to explain the temperature dependence predicted for the total DOS. In particular, in Figure 6 we show the evolution of the spectral density function with temperature predicted at three spe-

cific BZ points ($\vec{k}_1 = (0.55\pi, 0.55\pi)$, $\vec{k}_2 = (0.6\pi, 0.6\pi)$ and $\vec{k}_3 = (0.56\pi, 0.31\pi)$), which we could identify as exhibiting the largest non-trivial temperature dependent renormalization effects due to correlations (for details, see Supplementary Appendix B). Notice also that some non-Fermi liquid features are visible at specific BZ points at higher temperatures: in fact, Figure 6(b) shows that at $T = 100$ K the spectral density function at \vec{k}_2 is mostly dominated by the incoherent contribution, a strong reduction of the quasiparticle peak having taken place. Our prediction could be tested by temperature dependent ARPES experiments, and these effects should also be displayed by correlated multi-orbital models with more effective bands (though perhaps at larger correlation values). In Supplementary Appendix C.1, we discuss how doping affects the results discussed above for $n = 2$, and in particular how it reduces the non-trivial temperature dependent renormalization effects by correlations in the density of states, with differences between electron and hole doping. We also show how doping affects the k -dependence discussed for the parent compounds in connection with Fig. 6. Our results indicate that a subtle interplay between correlations, temperature and doping gives rise to the non-trivial temperature dependence effects in the spectral properties.

Finally, the quasiparticle weights $Z(k)$ at the Fermi level, defined as $Z^{-1}(\vec{k}) = 1 - \frac{\partial}{\partial \omega} \text{Re} \Sigma_c(\vec{k}, \omega)|_{\omega=0}$, are shown at different BZ points in Fig. 7, exhibiting the non-trivial effect of temperature along the BZ: clearly larger at some points like $k_3 = (0.56\pi, 0.31\pi)$, which would be interesting to probe by ARPES. Note that the mass renormalization ($\frac{m}{m^*} \propto Z$) obtained in our approach corresponds to a correlated metal, while the range of quasiparticle weights obtained along the BZ agrees with LDA+DMFT results⁵² who estimated a quasiparticle weight renormalization factor $Z \sim 0.8$ for $J = 0$, as well as with $T=0$ slave-spin mean-field studies of two- and four-orbital models.⁴¹

IV. CONCLUSIONS

Though a large amount of experimental and theoretical research work has been done since 2008, the true nature of electron correlations in ferropnictides remains an open question. Here, using a simplified model based on two correlated effective bands and an analytical approximation to decouple the equations of motion for the electron Green's functions, we determined the normal state spectral density function and the total density of states. With model parameters in the range relevant for iron-based superconductors, we could describe: (i) the momentum dependence measured in ARPES along $\Gamma - X$, and the main features along $\Gamma - M$; (ii) an asymmetric effect of electron and hole doping, with the characteristics observed in ARPES experiments. In particular, the band structure renormalization due to the correlation effects captured by our analytical approach, allows

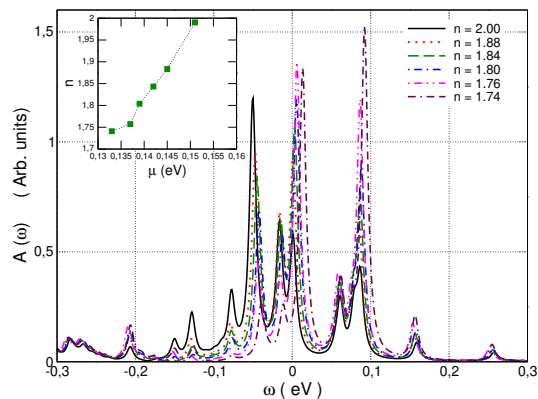


FIG. 7. Quasiparticle weights at the Fermi level, $Z(\vec{k})$, shown at a set BZ points (located as indicated in the inset), for temperatures: $T = 40, 60, 100$ K. $U = V = 3.5$ eV and other parameters as in Fig.1. $k_0 = (\pi/2, \pi/2)$, $k_1 = (0.55\pi, 0.55\pi)$, $k_2 = (0.6\pi, 0.6\pi)$, $k_3 = (0.56\pi, 0.31\pi)$, $k_4 = (\pi, 0.5\pi)$ and $k_5 = (0.5\pi, 0)$.

to obtain a direct agreement of our calculations with the experimental chemical potential shifts reported, with the correct order of magnitude in contrast to LDA calculations. (iii) We found that an important spectral weight reduction near the Fermi level takes place if temperature is increased, and the evolution with temperature of the total density of states which we predict is consistent with the relatively few available data from ARPES and hard X-ray photoemission experiments. (iv) The conduction electron mass renormalization obtained corresponds to a correlated metal, while the range of quasiparticle weights at the Fermi level which we obtain along the Brillouin zone agrees with theoretical LDA+DMFT results which estimated $Z \sim 0.8$ in the absence of Hund coupling.

Among the results obtained, we want to stress an interesting prediction which might be tested experimentally: our work not only predicts a non-trivial temperature dependence of the total density of states, due to correlation effects. We could trace the origin of this behaviour to specific Brillouin zone regions where the effect of temperature on the renormalization is amplified, by exploring the k-dependent self-energy obtained in our approach throughout the Brillouin zone. It would be interesting to have this prediction tested, by temperature dependent ARPES experiments in the specific BZ points we explicitly identified for undoped compounds.

Our calculated Green's functions might be also employed to evaluate other normal state physical properties of iron pnictides, at our level of approximation: which has the advantage of enabling to describe temperature and k-dependent results, in contrast to other theoretical techniques where the self-energy is local.

We have shown that our results describe well most of the main common features of the bulk electronic structure observed, not only 1111 and 122 ferropnictides, but also in FeSe compounds which we believe is related to the

fact that the two correlated effective bands of the model capture the relevant details of the 3d-Fe orbitals near the Fermi level, lying the As or Se orbitals further below in energy.

The simplified pnictides model and analytical approach used in the present work, are suitable for extensions to describe details of magnetotransport in FeSe compounds, as well as adapting them to describe electronic properties of BiS₂-based layered compounds. Our approach could also be useful to address the nature of correlations in Hund metals and its relationship with Mott-physics in other multi-orbital systems⁸⁶, problems we plan to study in the future.

V. ACKNOWLEDGMENTS

R.C. acknowledges I. Eremin for useful discussions on the manuscript. C.I.V. is Investigadora Científica of CONICET (Argentina). J.D.Q.F. has a fellowship from CONICET. C.I.V. acknowledges support from CONICET (PIP 0702) and ANPCyT (PICT'38357; PICT Redes'1776), and the hospitality of ICTP (International Centre for Theoretical Physics, Trieste) and Dipto. di Fisica, Università di Salerno, where part of this collaboration work was done. J.D.Q.F. acknowledges the hospitality of IIP (International Institute of Physics, Natal).

Appendix A: Analytical approximation: decoupling of the Green's function equations of motion.

As mentioned in section II B, for the model Hamiltonian given by Eqs. ??, 2 and 5 we calculated the equations of motion (EOM) of the Green's functions $G(\vec{k}, \omega)$ and $F(\vec{k}, \omega)$, respectively corresponding to c- and d-electrons defined in Eqs. 9 and 10, using Zubarev's formalism⁶⁷. We obtained the set of exact equations of motion detailed in Eqs. 12 and 13. Furthermore, the equations of motion for the three Γ_i ($i=1,3$) functions coupled to $G(\vec{k}, \omega)$, and for Γ_i ($i=4,6$) coupled to $F(\vec{k}, \omega)$, introduce coupling to new higher-order Green's functions in the problem. In this appendix we will detail the RPA-like analytical approximation used to obtain the Green's functions $G(\vec{k}, \omega)$ and $F(\vec{k}, \omega)$, required to calculate the spectral density and total density of states defined in Eqs. 7 and 11.

1. First order solution of EOM: Hartree-Fock decoupling.

First, we will explain how one could close and solve the coupled set of equations of motion in lowest order, which would correspond to the Hartree-Fock approximation.

The approximation to be used in Eqs. 12 and 13 for the Γ_i ($i = 1,6$) Green's functions which appear coupled to $G(\vec{k}, \omega)$ and $F(\vec{k}, \omega)$, respectively, basically consists in approximating Γ_i ($i = 1,6$) as proportional to $G(\vec{k}, \omega)$ and $F(\vec{k}, \omega)$, with mean values of the occupation numbers of the c- and d-bands appearing as proportionality factors, thus obtaining a closed system of equations of motion. Below, we show the approximation explicitly for $\Gamma_1(k_1, k_2, k, \omega)$:

$$\begin{aligned} \Gamma_1(k_1, k_2, k, \omega) &\equiv \Gamma_{\sigma, \bar{\sigma}, \bar{\sigma}}^{ccc}(k_1, k_2, k, \omega) = \\ &= \ll c_{k_2, \sigma} c_{k_1, \bar{\sigma}}^\dagger c_{k_1 - k_2 + k, \bar{\sigma}}; c_{k, \sigma}^\dagger \gg (\omega) \\ &\sim \langle c_{k_1, \bar{\sigma}}^\dagger c_{k_1 - k_2 + k, \bar{\sigma}} \rangle \ll c_{k_2, \sigma}; c_{k, \sigma}^\dagger \gg (\omega) \\ &\sim \langle c_{k_1, \bar{\sigma}}^\dagger c_{k_1 - k_2 + k, \bar{\sigma}} \rangle > \delta_{k_1, k_1 - k_2 + k} \ll c_{k_2, \sigma}; c_{k, \sigma}^\dagger \gg (\omega) \\ &\sim \langle n_{k_1, \bar{\sigma}} \rangle > \delta_{k, k_2} G_\sigma(k, \omega) \end{aligned} \quad (\text{A1})$$

where: $n_{k_1, \bar{\sigma}} = \langle c_{k_1, \bar{\sigma}}^\dagger c_{k_1, \bar{\sigma}} \rangle$.

Similarly, in this first level of approximation:

$$\begin{aligned} \Gamma_2(k_1, k_2, k, \omega) &\equiv \Gamma_{\sigma, \sigma, \sigma}^{cdd}(k_1, k_2, k, \omega) \\ &\sim \langle N_{k_1, \sigma} \rangle > \delta_{k, k_2} G_\sigma(k, \omega) \\ \Gamma_3(k_1, k_2, k, \omega) &\equiv \Gamma_{\sigma, \bar{\sigma}, \bar{\sigma}}^{cdd}(k_1, k_2, k, \omega) \\ &\sim \langle N_{k_1, \bar{\sigma}} \rangle > \delta_{k, k_2} G_\sigma(k, \omega) \end{aligned} \quad (\text{A2})$$

where: $N_{k_1, \sigma} = \langle d_{k_1, \sigma}^\dagger d_{k_1, \sigma} \rangle$.

Therefore, replacing this approximation for Γ_i ($i = 1,3$) in Eq. 12 one has:

$$\begin{aligned} [\omega - E_c(k)] G_\sigma(k, \omega) &= \frac{1}{2\pi} + \sum_{k_1, k_2} \frac{U}{N} \delta_{k_1, k_2} \langle n_{k_1, \bar{\sigma}} \rangle G_\sigma(k, \omega) \\ &+ \frac{V}{N} \delta_{k_2, k} (\langle N_{k_1, \bar{\sigma}} \rangle + \langle N_{k_1, \sigma} \rangle) G_\sigma(k, \omega) \end{aligned} \quad (\text{A3})$$

from which one directly obtains:

$$G_\sigma^{H.F.}(k, \omega) \sim \frac{1}{2\pi [\omega - E_c(k) - \sum_{k_1} (\frac{U}{N} \langle n_{k_1, \bar{\sigma}} \rangle + \frac{V}{N} \langle N_{k_1} \rangle)]} \quad (\text{A4})$$

where: $\langle N_{k_1} \rangle \equiv \langle N_{k_1, \uparrow} \rangle + \langle N_{k_1, \downarrow} \rangle$.

On the other hand, using this approximation for Γ_i (i

= 4,6) one has:

$$\begin{aligned} \Gamma_4(k_1, k_2, k, \omega) &\equiv \Gamma_{\sigma, \bar{\sigma}, \bar{\sigma}}^{ddd}(k_1, k_2, k, \omega) \\ &\sim \langle N_{k_1, \bar{\sigma}} \rangle > \delta_{k, k_2} F_\sigma(k, \omega) \\ \Gamma_5(k_1, k_2, k, \omega) &\equiv \Gamma_{\sigma, \sigma, \sigma}^{dcc}(k_1, k_2, k, \omega) \\ &\sim \langle n_{k_1, \sigma} \rangle > \delta_{k, k_2} F_\sigma(k, \omega) \\ \Gamma_6(k_1, k_2, k, \omega) &\equiv \Gamma_{\sigma, \bar{\sigma}, \bar{\sigma}}^{dcc}(k_1, k_2, k, \omega) \\ &\sim \langle n_{k_1, \bar{\sigma}} \rangle > \delta_{k, k_2} F_\sigma(k, \omega) \end{aligned} \quad (\text{A5})$$

which, by replacement in Eq. 13, leads to:

$$F_\sigma^{H.F.}(k, \omega) \sim \frac{1}{2\pi [\omega - E_d(k) - \sum_{k_1} (\frac{U}{N} \langle N_{k_1, \bar{\sigma}} \rangle + \frac{V}{N} \langle n_{k_1} \rangle)]} \quad (\text{A6})$$

Finally, considering that:

$$\frac{1}{N} \sum_{k_1} \langle n_{k_1, \bar{\sigma}} \rangle = \langle n_{i, \bar{\sigma}} \rangle \equiv \langle n_{c, \bar{\sigma}} \rangle \quad \forall i \quad (\text{A7})$$

$$\frac{1}{N} \sum_{k_1} \langle N_{k_1} \rangle = \langle N_i \rangle \equiv \langle n_d \rangle \quad \forall i \quad (\text{A8})$$

one can rewrite the Green's functions in this first order (Hartree-Fock) order of approximation as:

$$G_\sigma^{H.F.}(k, \omega) \cong \frac{1}{2\pi [\omega - E_c(k) - (U \langle n_{c, \bar{\sigma}} \rangle - V \langle n_d \rangle)]} \quad (\text{A9})$$

and,

$$F_\sigma^{H.F.}(k, \omega) \cong \frac{1}{2\pi [\omega - E_d(k) - (U \langle n_{d, \bar{\sigma}} \rangle - V \langle n_c \rangle)]} \quad (\text{A10})$$

2. Second-order solution of EOM: RPA decoupling

In the following, we will describe the second-order decoupling and solution of the equations of motion for $G(\vec{k}, \omega)$ and $F(\vec{k}, \omega)$, which we used to calculate all spectral density and total density of states results presented in Section III.

As mentioned above, the exact equation of motion for $G(\vec{k}, \omega)$, Eq. 12, involves sums over two k-indices of the three coupled Green's functions: Γ_i ($i=1,3$) defined in Eqs.14. Now, instead of approximating these coupled Green's functions directly in Eq. 12, as in the first order (HF) solution, we determine the three equations of motion for the Γ_i ($i=1,3$) Green's functions, respectively. Concretely, for $\Gamma_1(k_1, k_2, k, \omega) = \ll c_{k_2, \sigma} c_{k_1, \bar{\sigma}}^\dagger c_{k_1 - k_2 + k, \bar{\sigma}}; c_{k, \sigma}^\dagger \gg (\omega)$ we obtain the following equation of motion:

$$\begin{aligned} \omega \Gamma_1(k_1, k_2, k, \omega) &= \frac{\delta_{k, k_2}}{2\pi} \langle n_{k_1, \bar{\sigma}} \rangle + \\ &\ll [\Gamma_1(k_1, k_2, k), \mathcal{H}]; c_{k\sigma}^\dagger \gg (\omega) \end{aligned} \quad (\text{A11})$$

where $[\Gamma_1, \mathcal{H}] = [\Gamma_1, \mathcal{H}_0] + [\Gamma_1, V_{int}]$ introduces coupling of the EOM to new higher order Green's functions. In particular, the term $[\Gamma_1, \mathcal{H}_0]$ couples new Green's functions $\ll A; c_{k\sigma}^\dagger \gg$ where A involves three operator products: one creation and two annihilation ones, e.g.: $\Gamma_{\sigma, \bar{\sigma}, \bar{\sigma}}^{cdd}(k'_1, k'_2, k, \omega) \equiv \ll c_{k'_1, \bar{\sigma}}^\dagger c_{k'_1 - k_2 + k, \bar{\sigma}} c_{k'_2, \sigma}^\dagger; c_{k, \sigma}^\dagger \gg (\omega)$. On the other hand, the term $[\Gamma_1, V_{int}]$ in Eq. A11 couples four new higher order Green's functions, each involving five operator products in A : two creation and three annihilation ones, such as $c_\sigma c_\sigma^\dagger c_\sigma c_\sigma^\dagger c_\sigma c_\sigma^\dagger$, $c_\sigma c_\sigma^\dagger c_\sigma^\dagger d_\sigma^\dagger d_\sigma$ and $c_\sigma c_\sigma^\dagger c_\sigma^\dagger d_\sigma^\dagger d_\sigma$. Similar results are obtained when calculating the equations of motion for $\Gamma_2(k_1, k_2, k, \omega)$ and $\Gamma_3(k_1, k_2, k, \omega)$.

Analogously, the exact equation of motion for $F(\vec{k}, \omega)$, Eq. 13, involves sums over two k -indices of three coupled Green's functions: Γ_i ($i=4,6$) defined in Eqs.15, whose own equations of motion indirectly couple $F(\vec{k}, \omega)$ to new higher-order Green's functions in the problem.

To close the coupled set of equations of motion at this second-order level, we used the following approximation: all new higher-order Green's functions introduced in each subset of equations of motion for Γ_i ($i=1,3$), were approximated in mean-field in terms of Γ_i ($i=1,3$) and $G(\vec{k}, \omega)$ (introducing appropriate average values), yielding a 4×4 closed set of equations of motion. We proceeded likewise for the subset of equations for Γ_i ($i=4,6$) related to $F(\vec{k}, \omega)$.

To exemplify the decoupling scheme adopted to close the set of EOM at this level, below we show the approximation used for the higher-order Green's functions involving three operator products: $\Gamma_{\sigma, \bar{\sigma}, \bar{\sigma}}^{cdd}(k'_1, k'_2, k, \omega) = \ll c_{k'_2, \sigma} c_{k'_1, \bar{\sigma}}^\dagger c_{k'_1 - k_2 + k, \bar{\sigma}}; c_{k, \sigma}^\dagger \gg (\omega)$, according to the definition in Eq.16. Approximating this Green's function in mean field yields:

$$\begin{aligned} \Gamma_{\sigma, \bar{\sigma}, \bar{\sigma}}^{cdd}(k'_1, k'_2, k, \omega) &\simeq \langle c_{k'_1, \bar{\sigma}}^\dagger c_{k'_1 - k_2 + k, \bar{\sigma}} \rangle \ll c_{k'_2, \sigma}; c_{k, \sigma}^\dagger \gg (\omega) \\ &\simeq \delta_{k'_2, k} \langle n_{k'_1, \bar{\sigma}} \rangle \ll c_{k'_2, \sigma}; c_{k, \sigma}^\dagger \gg (\omega) \\ &\simeq \langle n_{k'_1, \bar{\sigma}} \rangle G_\sigma(k, \omega) \end{aligned}$$

Equation of motion for $\Gamma_1(k_1, k_2, k, \omega)$:

$$\begin{aligned} \omega \Gamma_1(k_1, k_2, k, \omega) &\simeq \frac{\delta_{k_2, k}}{2\pi} \langle n_{k_1, \bar{\sigma}} \rangle + [E_c(k_1 - k_2 + k) - E_c(k_1) + E_c(k_2) + U(n_c + 1)] \Gamma_1(k_1, k_2, k, \omega) \\ &+ \{2V \langle n_{k_1, \bar{\sigma}} \rangle n_d + (2 + \langle n_{k_1, \bar{\sigma}} \rangle) U n_c + U(\langle n_{k_1, \bar{\sigma}} \rangle - \langle n_{k_1 - k_2 + k, \bar{\sigma}} \rangle)\} G_\sigma(k, \omega) \\ &+ \frac{V}{N} (\langle n_{k_1, \bar{\sigma}} \rangle - \langle n_{k_1 - k_2 + k, \bar{\sigma}} \rangle) \left[\sum_{k'_1} \Gamma_2(k'_1, k_2, k, \omega) + \sum_{k'_1} \Gamma_3(k'_1, k_2, k, \omega) \right] \end{aligned} \quad (\text{A12})$$

Equation of motion for $\Gamma_2(k_1, k_2, k, \omega)$:

We now illustrate the decoupling of the higher-order Green's functions involving five operator products, by two examples: $\ll c_{k'_2, \sigma} c_{k'_1, \bar{\sigma}}^\dagger c_{k_2 - k'_2 + k'_1, \bar{\sigma}} c_{k_1 - k_2 + k, \bar{\sigma}}; c_{k, \sigma}^\dagger \gg$ and $\ll c_{k'_2, \sigma} c_{k'_1, \bar{\sigma}}^\dagger c_{k_1 - k_2 + k, \bar{\sigma}} d_{k'_1, \sigma}^\dagger d_{k_2 - k'_2 + k'_1, \sigma}; c_{k, \sigma}^\dagger \gg$. Approximating these Green's functions in mean field yields:

$$\begin{aligned} &\ll c_{k'_2, \sigma} c_{k'_1, \bar{\sigma}}^\dagger c_{k_2 - k'_2 + k'_1, \bar{\sigma}} c_{k_1 - k_2 + k, \bar{\sigma}}; c_{k, \sigma}^\dagger \gg (\omega) \\ &\simeq \langle c_{k'_1, \bar{\sigma}}^\dagger c_{k_2 - k'_2 + k'_1, \bar{\sigma}} \rangle \ll c_{k'_2, \sigma} c_{k_1 - k_2 + k, \bar{\sigma}}; c_{k, \sigma}^\dagger \gg (\omega) \\ &+ \langle c_{k_1, \bar{\sigma}}^\dagger c_{k_1 - k_2 + k, \bar{\sigma}} \rangle \ll c_{k'_2, \sigma} c_{k_1 - k_2 + k, \bar{\sigma}}; c_{k, \sigma}^\dagger \gg (\omega) \\ &\simeq \delta_{k_1, k'_2} \langle n_{k'_1, \bar{\sigma}} \rangle \Gamma_{\sigma, \bar{\sigma}, \bar{\sigma}}^{ccc}(k_1, k'_2, k, \omega) \\ &\quad + \delta_{k, k_2} \langle n_{k_1, \bar{\sigma}} \rangle \Gamma_{\sigma, \bar{\sigma}, \bar{\sigma}}^{ccc}(k'_1, k'_2, k, \omega) \\ &\simeq \delta_{k_1, k'_2} \langle n_{k'_1, \bar{\sigma}} \rangle \Gamma_1(k_1, k'_2, k, \omega) + \delta_{k, k_2} \langle n_{k_1, \bar{\sigma}} \rangle \Gamma_1(k'_1, k'_2, k, \omega) \end{aligned}$$

and,

$$\begin{aligned} &\ll c_{k'_2, \sigma} c_{k'_1, \bar{\sigma}}^\dagger c_{k_1 - k_2 + k, \bar{\sigma}} d_{k'_1, \sigma}^\dagger d_{k_2 - k'_2 + k'_1, \sigma}; c_{k, \sigma}^\dagger \gg (\omega) \\ &\simeq \langle c_{k_1, \bar{\sigma}}^\dagger c_{k_1 - k_2 + k, \bar{\sigma}} \rangle \ll c_{k'_2, \sigma} d_{k'_1, \sigma}^\dagger d_{k_2 - k'_2 + k'_1, \sigma}; c_{k, \sigma}^\dagger \gg (\omega) \\ &+ \langle d_{k'_1, \sigma}^\dagger d_{k_2 - k'_2 + k'_1, \sigma} \rangle \ll c_{k'_2, \sigma} c_{k_1 - k_2 + k, \bar{\sigma}}; c_{k, \sigma}^\dagger \gg (\omega) \\ &\simeq \delta_{k_2, k} \langle n_{k_1, \bar{\sigma}} \rangle \Gamma_2(k'_1, k'_2, k, \omega) + \delta_{k_2, k'_2} \langle N_{k'_1, \sigma} \rangle \Gamma_1(k_1, k'_2, k, \omega) \end{aligned}$$

All other higher-order Green's functions were decoupled following the same procedure. We proceeded likewise for the subset of equations for Γ_i ($i=4,6$) related to $F(\vec{k}, \omega)$.

Finally, the equations of motion for the six Green's functions Γ_i ($i=1,6$) in RPA approximation read:

$$\begin{aligned}
\omega\Gamma_2(k_1, k_2, k, \omega) &\cong \frac{\delta_{k_2, k}}{2\pi} \langle N_{k_1, \sigma} \rangle + [E_d(k_1 - k_2 + k) - E_d(k_1) + E_c(k_2) + Un_c + 2n_d(U + V) - V] \Gamma_2(k_1, k_2, k, \omega) \\
&\quad + \{(U - V) \langle N_{k_1, \sigma} \rangle + 2V \langle N_{k_1, \sigma} \rangle n_d - V(\langle N_{k_1, \sigma} \rangle - \langle N_{k_1 - k_2 + k, \sigma} \rangle) + V\} G_\sigma(k, \omega) \\
&\quad + \frac{V}{N} (\langle N_{k_1, \sigma} \rangle - \langle N_{k_1 - k_2 + k, \sigma} \rangle) \left[\sum_{k'_1} \Gamma_1(k'_1, k_2, k, \omega) \right] + \frac{U}{N} (\langle N_{k_1, \sigma} \rangle - \langle N_{k_1 - k_2 + k, \sigma} \rangle) \left[\sum_{k'_1} \Gamma_3(k'_1, k_2, k, \omega) \right] \quad (\text{A13})
\end{aligned}$$

Equation of motion for $\Gamma_3(k_1, k_2, k, \omega)$:

$$\begin{aligned}
\omega\Gamma_3(k_1, k_2, k, \omega) &\cong \frac{\delta_{k_2, k}}{2\pi} \langle N_{k_1, \bar{\sigma}} \rangle + [E_d(k_1 - k_2 + k) - E_d(k_1) + E_c(k_2) + Un_c + 2Vn_d + V] \Gamma_3(k_1, k_2, k, \omega) \\
&\quad + \{U \langle N_{k_1, \bar{\sigma}} \rangle n_c + V(1 - \langle n_{k_1, \bar{\sigma}} \rangle - \langle n_{k_1 - k_2 + k, \bar{\sigma}} \rangle) n_d + V(\langle n_{k_1, \bar{\sigma}} \rangle)\} G_\sigma(k, \omega) \\
&\quad + \frac{V}{N} (\langle N_{k_1, \bar{\sigma}} \rangle - \langle N_{k_1 - k_2 + k, \bar{\sigma}} \rangle) \left[\sum_{k'_1} \Gamma_1(k'_1, k_2, k, \omega) \right] + \frac{U}{N} (\langle N_{k_1, \bar{\sigma}} \rangle - \langle N_{k_1 - k_2 + k, \bar{\sigma}} \rangle) \left[\sum_{k'_1} \Gamma_2(k'_1, k_2, k, \omega) \right] \quad (\text{A14})
\end{aligned}$$

Equation of motion for $\Gamma_4(k_1, k_2, k, \omega)$:

$$\begin{aligned}
\omega\Gamma_4(k_1, k_2, k, \omega) &\cong \frac{\delta_{k_2, k}}{2\pi} \langle N_{k_1, \bar{\sigma}} \rangle + [E_d(k_1 - k_2 + k) - E_d(k_1) + E_d(k_2) + U(n_d + 1)] \Gamma_4(k_1, k_2, k, \omega) \\
&\quad + \{2V \langle N_{k_1, \bar{\sigma}} \rangle n_c + (2 + \langle N_{k_1, \bar{\sigma}} \rangle) Un_d + U(\langle N_{k_1, \bar{\sigma}} \rangle - \langle N_{k_1 - k_2 + k, \bar{\sigma}} \rangle)\} F_\sigma(k, \omega) \\
&\quad + \frac{V}{N} (\langle N_{k_1, \bar{\sigma}} \rangle - \langle N_{k_1 - k_2 + k, \bar{\sigma}} \rangle) \left[\sum_{k'_1} \Gamma_5(k'_1, k_2, k, \omega) + \sum_{k'_1} \Gamma_6(k'_1, k_2, k, \omega) \right] \quad (\text{A15})
\end{aligned}$$

Equation of motion for $\Gamma_5(k_1, k_2, k, \omega)$:

$$\begin{aligned}
\omega\Gamma_5(k_1, k_2, k, \omega) &\cong \frac{\delta_{k_2, k}}{2\pi} \langle n_{k_1, \sigma} \rangle + [E_c(k_1 - k_2 + k) - E_c(k_1) + E_d(k_2) + Un_d + 2n_c(U + V) - V] \Gamma_5(k_1, k_2, k, \omega) \\
&\quad + \{(U - V) \langle n_{k_1, \sigma} \rangle + 2V \langle n_{k_1, \sigma} \rangle n_c - V(\langle n_{k_1, \sigma} \rangle - \langle n_{k_1 - k_2 + k, \sigma} \rangle) + V\} F_\sigma(k, \omega) \\
&\quad + \frac{V}{N} (\langle n_{k_1, \sigma} \rangle - \langle n_{k_1 - k_2 + k, \sigma} \rangle) \left[\sum_{k'_1} \Gamma_4(k'_1, k_2, k, \omega) \right] + \frac{U}{N} (\langle n_{k_1, \sigma} \rangle - \langle n_{k_1 - k_2 + k, \sigma} \rangle) \left[\sum_{k'_1} \Gamma_6(k'_1, k_2, k, \omega) \right] \quad (\text{A16})
\end{aligned}$$

Equation of motion for $\Gamma_6(k_1, k_2, k, \omega)$:

$$\begin{aligned}
\omega\Gamma_6(k_1, k_2, k, \omega) &\cong \frac{\delta_{k_2, k}}{2\pi} \langle n_{k_1, \bar{\sigma}} \rangle + [E_c(k_1 - k_2 + k) - E_c(k_1) + E_d(k_2) + Un_d + 2Vn_c + V] \Gamma_6(k_1, k_2, k, \omega) \\
&\quad + \{U \langle n_{k_1, \bar{\sigma}} \rangle n_d + V(1 - \langle N_{k_1, \bar{\sigma}} \rangle - \langle N_{k_1 - k_2 + k, \bar{\sigma}} \rangle) n_c + V(\langle N_{k_1, \bar{\sigma}} \rangle)\} F_\sigma(k, \omega) \\
&\quad + \frac{V}{N} (\langle n_{k_1, \bar{\sigma}} \rangle - \langle n_{k_1 - k_2 + k, \bar{\sigma}} \rangle) \left[\sum_{k'_1} \Gamma_4(k'_1, k_2, k, \omega) \right] + \frac{U}{N} (\langle n_{k_1, \bar{\sigma}} \rangle - \langle n_{k_1 - k_2 + k, \bar{\sigma}} \rangle) \left[\sum_{k'_1} \Gamma_5(k'_1, k_2, k, \omega) \right] \quad (\text{A17})
\end{aligned}$$

Notice that this RPA-like approximation involves a second-order closed set of equations for $G_\sigma(k, \omega)$, and double k -index summations of Γ_1 , Γ_2 and Γ_3 ; and an analogous one for $F_\sigma(k, \omega)$, Γ_4 , Γ_5 and Γ_6 . Below we explain how we could solve these two sets of coupled equations of motion, and detail the Green's functions $G(\vec{k}, \omega)$ and $F(\vec{k}, \omega)$ obtained, required to calculate the spectral density and total density of states results presented in Section III.

a. Solution of the equations of motion determining $G_\sigma(k, \omega)$.

The keypoint to close the EOM system at this second-order level, enabling to determine $G_\sigma(k, \omega)$ from Eq. 12 using the RPA-coupled set of Eqs. A12, A13 and A14, is that only BZ summations over k_1 and k_2 of the $\Gamma_i(k_1, k_2, k)$

($i=1,3$) functions appear in Eq. 12. So that, appropriately (double) summing over the BZ the set of coupled set of equations, one can effectively extract $G_\sigma(k, \omega)$ at a fixed k as we explain in the following.

It is useful to introduce the following notation:

$$\Phi_i(k_2, k, \omega) \equiv \sum_{k_1} \Gamma_i(k_1, k_2, k, \omega) \quad , \quad i = 1, 3 \quad (\text{A18})$$

which allows to rewrite Eqs.A12, A13 and A14 as follows:

$$\begin{aligned} \Gamma_1(k_1, k_2, k, \omega) &= A_1 + B_1 G_\sigma(k, \omega) + C_1 [\Phi_2(k_2, k, \omega) + \Phi_3(k_2, k, \omega)] \\ \Gamma_2(k_1, k_2, k, \omega) &= A_2 + B_2 G_\sigma(k, \omega) + C_2 \left[\left(\frac{V}{N} \right) \Phi_1(k_2, k, \omega) + \left(\frac{U}{N} \right) \Phi_3(k_2, k, \omega) \right] \\ \Gamma_3(k_1, k_2, k, \omega) &= A_3 + B_3 G_\sigma(k, \omega) + C_3 \left[\left(\frac{V}{N} \right) \Phi_1(k_2, k, \omega) + \left(\frac{U}{N} \right) \Phi_2(k_2, k, \omega) \right] \end{aligned} \quad (\text{A19})$$

where the coefficients A_i , B_i and C_i are:

$$\begin{aligned} A_1 &= \frac{\langle n_{k_1, \bar{\sigma}} \rangle}{2\pi [\omega - E_c(k_2) - U(n_c + 1)]} \\ A_2 &= \frac{\langle N_{k_1, \sigma} \rangle}{2\pi [\omega - E_c(k_2) - U n_c - 2n_d(U + V) + V]} \\ A_3 &= \frac{\langle N_{k_1, \bar{\sigma}} \rangle}{2\pi [\omega - E_c(k_2) - U n_c - 2V n_d - V]} \\ B_1 &= \frac{\{2V \langle n_{k_1, \bar{\sigma}} \rangle n_d + (2 + \langle n_{k_1, \bar{\sigma}} \rangle) U n_c + U(\langle n_{k_1, \bar{\sigma}} \rangle - \langle n_{k_1 - k_2 + k, \bar{\sigma}} \rangle)\}}{\omega - \omega_1} \\ B_2 &= \frac{\{(U - V) \langle N_{k_1, \sigma} \rangle + 2V \langle N_{k_1, \sigma} \rangle n_d - V(\langle N_{k_1, \sigma} \rangle - \langle N_{k_1 - k_2 + k, \sigma} \rangle) + V\}}{\omega - \omega_2} \\ B_3 &= \frac{\{U \langle N_{k_1, \bar{\sigma}} \rangle n_c + V(1 - \langle n_{k_1, \bar{\sigma}} \rangle - \langle n_{k_1 - k_2 + k, \bar{\sigma}} \rangle) n_d + V \langle n_{k_1, \bar{\sigma}} \rangle\}}{\omega - \omega_3} \\ C_1 &= \frac{\frac{V}{N} [\langle n_{k_1, \bar{\sigma}} \rangle - \langle n_{k_1 - k_2 + k, \bar{\sigma}} \rangle]}{\omega - \omega_1} \\ C_2 &= \frac{[\langle N_{k_1, \sigma} \rangle - \langle N_{k_1 - k_2 + k, \sigma} \rangle]}{\omega - \omega_2} \\ C_3 &= \frac{[\langle N_{k_1, \bar{\sigma}} \rangle - \langle N_{k_1 - k_2 + k, \bar{\sigma}} \rangle]}{\omega - \omega_3} \end{aligned}$$

and,

$$\begin{aligned} \omega_1 &= [E_c(k_1 - k_2 + k) - E_c(k_1) + E_c(k_2) + U(n_c + 1)] \\ \omega_2 &= [E_d(k_1 - k_2 + k) - E_d(k_1) + E_c(k_2) + U n_c + 2n_d(U + V) - V] \\ \omega_3 &= [E_d(k_1 - k_2 + k) - E_d(k_1) + E_c(k_2) + U n_c + 2V n_d + V] \end{aligned}$$

Notice that if Eqs.A19 are BZ summed over k_1 , each of the $\Phi_i(k_2, k)$ can be derived in terms of $G_\sigma(k, \omega)$ and coefficients involving the temperature dependant-fillings, the effective band structure and the model's correlation parameters.

Meanwhile, if one introduces the notation:

$$\Theta_i(k) \equiv \sum_{k_1, k_2} \Gamma_i(k_1, k_2, k, \omega) \equiv \sum_{k_2} \Phi_i(k_2, k, \omega) \quad , \quad i = 1, 3 \quad (\text{A20})$$

Eq. 12 can be rewritten as:

$$[\omega - E_c(k)] G_\sigma(k, \omega) = \frac{1}{2\pi} + \left[\frac{U}{N} \Theta_1(k, \omega) + \frac{V}{N} \Theta_2(k, \omega) + \frac{V}{N} \Theta_3(k, \omega) \right] \quad (\text{A21})$$

Performing the k_2 summations in Eq. A20, all $\Theta_i(k)$ can be expressed in terms of $G_\sigma(k, \omega)$ and coefficients involving the temperature dependant-fillings, the effective and the model's correlation parameters, so that one can finally solve for $G_\sigma(k, \omega)$. We find the following expression for $G(\vec{k}, \omega)$, related to the c -electrons in our model, in this RPA- level approximation:

$$G_\sigma^{RPA}(k, \omega) \cong \frac{\frac{1}{2\pi} + \sum_{k_2} \left\{ \frac{U}{N} \left(\frac{Y_1}{X_1} \right) + \frac{V}{N} \left[\frac{Y_2}{X_2} + [A_3]_{k_1} + [C_3]_{k_1} \left(\frac{Y_1}{X_1} + \frac{Y_2}{X_2} \right) \right] \right\}}{\omega - E_c(k) - \sum_{k_2} \left\{ \frac{U}{N} \left(\frac{Z_1}{X_1} \right) + \frac{V}{N} \left[\frac{Z_2}{X_2} + [B_3]_{k_1} + [C_3]_{k_1} \left(\frac{Z_1}{X_1} + \frac{Z_2}{X_2} \right) \right] \right\}} \quad (\text{A22})$$

where, denoting: $[A]_{k_1} \equiv \sum_{k_1} A$, one has:

$$\begin{aligned} X_1(k_2, k) &= \left(1 - \frac{U}{N} [C_2]_{k_1} [C_3]_{k_1} \right) (1 - [C_1]_{k_1} [C_3]_{k_1}) - [C_1]_{k_1} \left(\frac{U}{N} [C_3]_{k_1} + 1 \right) \left(\frac{U}{N} [C_3]_{k_1} + \frac{V}{N} \right) [C_2]_{k_1} \\ Y_1(k_2, k) &= \left(1 - \frac{U}{N} [C_2]_{k_1} [C_3]_{k_1} \right) ([A_1]_{k_1} + [A_3]_{k_1} [C_1]_{k_1}) + \left([A_2]_{k_1} + \frac{U}{N} [C_2]_{k_1} [A_3]_{k_1} \right) [C_1]_{k_1} \left(\frac{U}{N} [C_3]_{k_1} + 1 \right) \\ Z_1(k_2, k) &= \left(1 - \frac{U}{N} [C_2]_{k_1} [C_3]_{k_1} \right) ([B_1]_{k_1} + [B_3]_{k_1} [C_1]_{k_1}) + [B_2]_{k_1} + \frac{U}{N} [C_2]_{k_1} [B_3]_{k_1} \\ \\ X_2(k_2, k) &= (1 - [C_1]_{k_1} [C_3]_{k_1}) \left(1 - \frac{U}{N} [C_2]_{k_1} [C_3]_{k_1} \right) - \left(\frac{U}{N} [C_3]_{k_1} + V \right) [C_2]_{k_1} [C_1]_{k_1} ([C_3]_{k_1} + 1) \\ Y_2(k_2, k) &= (1 - [C_1]_{k_1} [C_3]_{k_1}) \left([A_2]_{k_1} + \frac{U}{N} [C_2]_{k_1} [A_3]_{k_1} \right) + \left(\frac{U}{N} [C_3]_{k_1} + V \right) [C_2]_{k_1} ([A_1]_{k_1} + [A_3]_{k_1} [C_1]_{k_1}) \\ Z_2(k_2, k) &= (1 - [C_1]_{k_1} [C_3]_{k_1}) \left([B_2]_{k_1} + \frac{U}{N} [C_2]_{k_1} [B_3]_{k_1} \right) + \left(\frac{U}{N} [C_3]_{k_1} + V \right) [C_2]_{k_1} ([B_1]_{k_1} + [B_3]_{k_1} [C_1]_{k_1}) \end{aligned}$$

b. Solution of the equations of motion determining $F_\sigma(k, \omega)$.

We proceeded likewise for the subset of equations for Γ_i ($i = 4..6$) coupled to $F_\sigma(k, \omega)$:

$$\begin{aligned} \Gamma_4(k_1, k_2, k, \omega) &= A_1^* + B_1^* F_\sigma(k, \omega) + C_1^* [\Phi_5(k_2, k, \omega) + \Phi_6(k_2, k, \omega)] \\ \Gamma_5(k_1, k_2, k, \omega) &= A_2^* + B_2^* F_\sigma(k, \omega) + C_2^* \left[\left(\frac{V}{N} \right) \Phi_4(k_2, k, \omega) + \left(\frac{U}{N} \right) \Phi_6(k_2, k, \omega) \right] \\ \Gamma_6(k_1, k_2, k, \omega) &= A_3^* + B_3^* F_\sigma(k, \omega) + C_3^* \left[\left(\frac{V}{N} \right) \Phi_4(k_2, k, \omega) + \left(\frac{U}{N} \right) \Phi_5(k_2, k, \omega) \right] \end{aligned} \quad (\text{A23})$$

where,

$$\begin{aligned} A_1^* &= \frac{\langle N_{k_1, \bar{\sigma}} \rangle}{2\pi [\omega - E_d(k_2) - U(n_d + 1)]} \\ A_2^* &= \frac{\langle n_{k_1, \sigma} \rangle}{2\pi [\omega - E_d(k_2) - U n_d - 2n_c(U + V) + V]} \\ A_3^* &= \frac{\langle n_{k_1, \bar{\sigma}} \rangle}{2\pi [\omega - E_d(k_2) - U n_d - 2V n_c - V]} \\ \\ B_1^* &= \frac{\{2V \langle N_{k_1, \bar{\sigma}} \rangle n_c + (2 + \langle N_{k_1, \bar{\sigma}} \rangle) U n_d + U (\langle N_{k_1, \bar{\sigma}} \rangle - \langle N_{k_1 - k_2 + k, \bar{\sigma}} \rangle)\}}{\omega - \omega_1^*} \\ B_2^* &= \frac{\{(U - V) \langle N_{k_1, \sigma} \rangle + 2V \langle n_{k_1, \sigma} \rangle n_c - V (\langle n_{k_1, \sigma} \rangle - \langle n_{k_1 - k_2 + k, \sigma} \rangle) + V\}}{\omega - \omega_2^*} \\ B_3^* &= \frac{\{U \langle n_{k_1, \bar{\sigma}} \rangle n_d + V (1 - \langle N_{k_1, \bar{\sigma}} \rangle - \langle N_{k_1 - k_2 + k, \bar{\sigma}} \rangle) n_c + V (\langle N_{k_1, \bar{\sigma}} \rangle)\}}{\omega - \omega_3^*} \end{aligned}$$

$$\begin{aligned}
C_1^* &= \frac{V}{N} \frac{[\langle N_{k_1, \vec{\sigma}} \rangle - \langle N_{k_1 - k_2 + k, \vec{\sigma}} \rangle]}{\omega - \omega_1^*} \\
C_2^* &= \frac{[\langle n_{k_1, \sigma} \rangle - \langle n_{k_1 - k_2 + k, \sigma} \rangle]}{\omega - \omega_2^*} \\
C_3^* &= \frac{[\langle n_{k_1, \vec{\sigma}} \rangle - \langle n_{k_1 - k_2 + k, \vec{\sigma}} \rangle]}{\omega - \omega_3^*}
\end{aligned}$$

$$\begin{aligned}
\omega_1^* &= [E_d(k_1 - k_2 + k) - E_d(k_1) + E_d(k_2) + U(n_d + 1)] \\
\omega_2^* &= [E_c(k_1 - k_2 + k) - E_c(k_1) + E_d(k_2) + Un_d + 2n_c(U + V) - V] \\
\omega_3^* &= [E_c(k_1 - k_2 + k) - E_c(k_1) + E_d(k_2) + Un_d + 2Vn_c + V]
\end{aligned}$$

Carrying out the summations over \vec{k}_1 and \vec{k}_2 BZ points in the set of equations in Eq. A23 and Eq.13, we analogously find an expression for the Green's function $F_\sigma(k, \omega)$ corresponding to the d-electrons, in this RPA-level approximation:

$$F_\sigma^{RPA}(k, \omega) \cong \frac{\frac{1}{2\pi} + \sum_{k_2} \left\{ \frac{U}{N} \left(\frac{Y_1^*}{X_1^*} \right) + \frac{V}{N} \left[\frac{Y_2^*}{X_2^*} + [A_3^*]_{k_1} + [C_3^*]_{k_1} \left(\frac{Y_1^*}{X_1^*} + \frac{Y_2^*}{X_2^*} \right) \right] \right\}}{\omega - E_d(k) - \sum_{k_2} \left\{ \frac{U}{N} \left(\frac{Z_1^*}{X_1^*} \right) + \frac{V}{N} \left[\frac{Z_2^*}{X_2^*} + [B_3^*]_{k_1} + [C_3^*]_{k_1} \left(\frac{Z_1^*}{X_1^*} + \frac{Z_2^*}{X_2^*} \right) \right] \right\}} \quad (\text{A24})$$

where:

$$\begin{aligned}
X_1^*(k_2, k) &= \left(1 - \frac{U}{N} [C_2^*]_{k_1} [C_3^*]_{k_1} \right) (1 - [C_1^*]_{k_1} [C_3^*]_{k_1}) - [C_1^*]_{k_1} \left(\frac{U}{N} [C_3^*]_{k_1} + 1 \right) \left(\frac{U}{N} [C_3^*]_{k_1} + \frac{V}{N} \right) [C_2^*]_{k_1} \\
Y_1^*(k_2, k) &= \left(1 - \frac{U}{N} [C_2^*]_{k_1} [C_3^*]_{k_1} \right) ([A_1^*]_{k_1} + [A_3^*]_{k_1} [C_1^*]_{k_1}) + \left([A_2^*]_{k_1} + \frac{U}{N} [C_2^*]_{k_1} [A_3^*]_{k_1} \right) [C_1^*]_{k_1} \left(\frac{U}{N} [C_3^*]_{k_1} + 1 \right) \\
Z_1^*(k_2, k) &= \left(1 - \frac{U}{N} [C_2^*]_{k_1} [C_3^*]_{k_1} \right) ([B_1^*]_{k_1} + [B_3^*]_{k_1} [C_1^*]_{k_1}) + [B_2^*]_{k_1} + \frac{U}{N} [C_2^*]_{k_1} [B_3^*]_{k_1} \\
X_2^*(k_2, k) &= (1 - [C_1^*]_{k_1} [C_3^*]_{k_1}) \left(1 - \frac{U}{N} [C_2^*]_{k_1} [C_3^*]_{k_1} \right) - \left(\frac{U}{N} [C_3^*]_{k_1} + V \right) [C_2^*]_{k_1} [C_1^*]_{k_1} ([C_3^*]_{k_1} + 1) \\
Y_2^*(k_2, k) &= (1 - [C_1^*]_{k_1} [C_3^*]_{k_1}) \left([A_2^*]_{k_1} + \frac{U}{N} [C_2^*]_{k_1} [A_3^*]_{k_1} \right) + \left(\frac{U}{N} [C_3^*]_{k_1} + V \right) [C_2^*]_{k_1} ([A_1^*]_{k_1} + [A_3^*]_{k_1} [C_1^*]_{k_1}) \\
Z_2^*(k_2, k) &= (1 - [C_1^*]_{k_1} [C_3^*]_{k_1}) \left([B_2^*]_{k_1} + \frac{U}{N} [C_2^*]_{k_1} [B_3^*]_{k_1} \right) + \left(\frac{U}{N} [C_3^*]_{k_1} + V \right) [C_2^*]_{k_1} ([B_1^*]_{k_1} + [B_3^*]_{k_1} [C_1^*]_{k_1})
\end{aligned}$$

Appendix B: Analysis of the k-dependent self-energy

To better assess the nature of the second order (RPA-like) approximation which we used to decouple the equations of motion and determine the relevant Green's functions, yielding the spectral density and total density of states of our model, in the following we present an analysis of the self-energies for *c* and *d* electrons obtained in our approach, focusing on the k-dependence and the temperature dependence.

Using Dyson's equation, one can determine the second order self-energy related to each electron band as follows:

$$\Sigma_c(k, \omega) = G^0(k, \omega)^{-1} - G^{RPA}(k, \omega)^{-1} \quad (\text{B1})$$

$$\Sigma_d(k, \omega) = F^0(k, \omega)^{-1} - F^{RPA}(k, \omega)^{-1} \quad (\text{B2})$$

where, $G^0(k, \omega)$ and $F^0(k, \omega)$ represent the retarded non-interacting Green's functions corresponding to the two bare effective bands: for the uncorrelated *c*- and *d*-bands, respectively, $G^0(k, \omega)^{-1} = \omega - E_c(\vec{k})$ and $F^0(k, \omega)^{-1} = \omega - E_d(\vec{k})$. Meanwhile: $G^{RPA}(k, \omega)$ and $F^{RPA}(k, \omega)$ were defined in Eqs. A22 and A24 of Appendix A.

First, notice that the self-energy in Hartree-Fock approximation for the *c*- and *d*-orbital Green's functions (Eqs. A4 and A6) is independent of crystal momentum *k* and energy.

Therefore, in this appendix we present our results obtained evaluating in second order level of approximation (as detailed in Appendix A) the real and imaginary parts of the self-energies defined above, corresponding to the retarded electron Green's functions of eqs. A22 and A24. Our results confirm that in our RPA-like approach, the self-energies exhibit clear renormalization effects due to

the correlations included: with non-trivial crystal momentum, temperature, doping, and energy dependence.

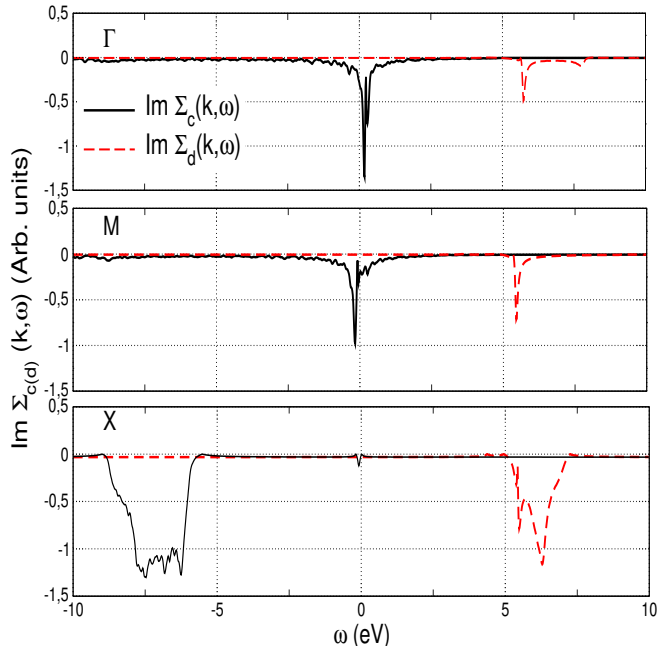


FIG. 8. Imaginary part of the c- and d-band self-energies as a function of energy (w.r. to the Fermi level), at the following symmetry points of the square lattice Brillouin zone: Γ ($\vec{k} = (0, 0)$), M ($\vec{k} = (\pi, \pi)$) and X ($\vec{k} = (\pi, 0)$). Parameters: $U = V = 3.5$, $n_c = 1.45$ and $n_d = 0.56$, $T = 20K$. Bare effective band tight-binding parameters as in Ref. 30

In the following, our results will be presented in a series of figures, in particular exhibiting the diversity of the temperature dependence which is obtained at different k -points in the Brillouin zone. As general consistency checks of our results, notice: the correct (negative) sign exhibited by the imaginary parts of the electron self-energies, while the real parts of the self-energies, which represent the energy shifts renormalizing the bare electron energies in our approximation, are correctly Kramers-Kronig related to the respective imaginary parts.

1. Momentum dependence of $\Sigma_c(k, \omega)$ and $\Sigma_d(k, \omega)$

First, we exemplify the momentum dependence of the imaginary part of the two self-energies $\Sigma_c(k, \omega)$ and $\Sigma_d(k, \omega)$ in our approximation. In Fig. 8, we show the imaginary parts of the two self-energies at the three relevant high symmetry BZ points of the square lattice, usually probed by ARPES. The upper two panels show that at the Brillouin zone centre (Γ) and at M , the c-band is mainly renormalized around the Fermi level, while the d-band is mostly renormalized far away from the Fermi level, at energies close to the bare band edges ($\omega > 5\text{eV}$).

The lower panel depicts the imaginary parts of the two self-energies at X ($\vec{k} = (\pi, 0)$): which noticeably differs from the previous cases. At X the renormalization is relevant mostly near the band edges of the bare electronic structure, while near the Fermi level the renormalization at X is not significant.

In the rest of this appendix, we will focus on the renormalization of the energies obtained near the Fermi level, and therefore center our discussion on $\Sigma_c(\vec{k}, \omega)$.

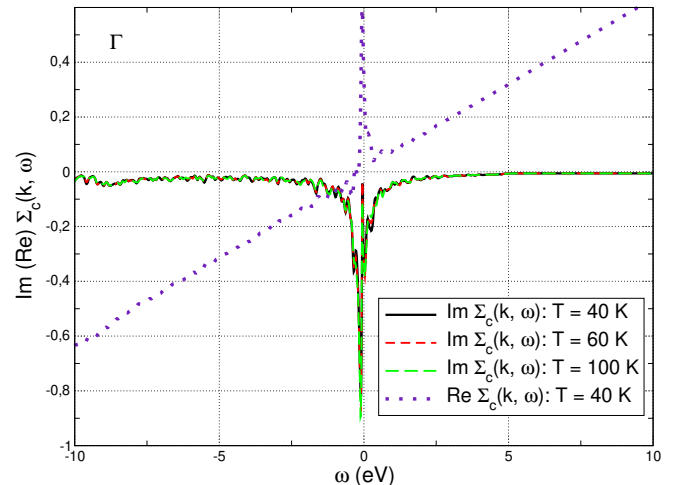


FIG. 9. Temperature dependence of the imaginary part of $\Sigma_c(k, \omega)$ at Γ . T as labelled in the figure, other parameters as in Fig. 8.

2. Temperature dependence of the self-energy

a. Imaginary part of the self-energy

Now, we will focus on the evolution with temperature of the imaginary part of $\Sigma_c(\vec{k}, \omega)$, in particular fixing \vec{k} at the relevant high-symmetry points of the BZ studied by ARPES experiments, and also at other BZ points: in which we found that the temperature dependence of the renormalization was larger and non-trivial (not the expected behaviour resulting from $f_{FD}(\omega)$).

Fig. 9 shows that at Γ the renormalization of the self-energy is almost independent of temperature. We found that also at M and X the effect of temperature on the renormalization is almost irrelevant. This negligible temperature dependence of the self-energy at the high symmetry BZ points explored by ARPES, Γ , M and X , explains the spectral density function results presented in Figs. 10 and 11 of Section ??.

But from the total density of states results in Fig. 9 of Section ??, we know that non-trivial relevant temperature-dependent effects indeed appear when the contributions of the whole BZ are taken into account. Therefore, we used a grid to explore the temperature

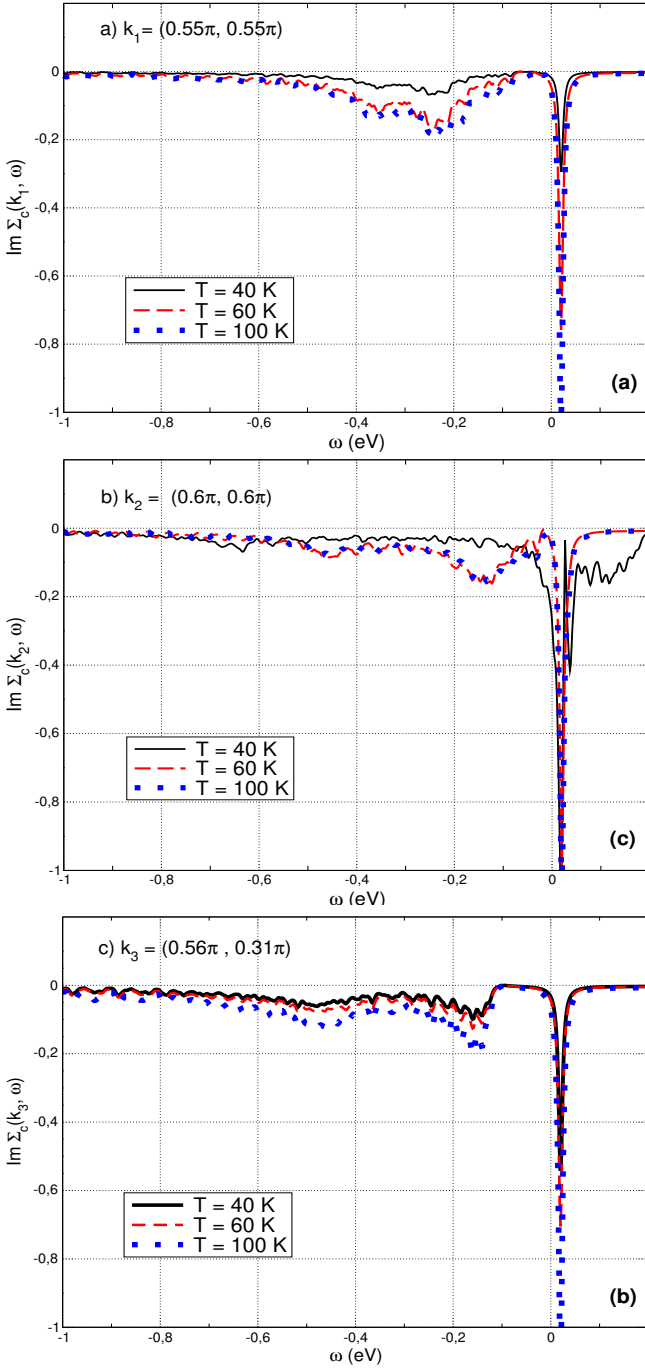


FIG. 10. Temperature dependence of the imaginary part of $\Sigma_c(k, \omega)$ at the BZ points respectively indicated in the plots. T as labelled in the figure, other parameters as in Fig. 8.

dependence of the renormalization at different points of the BZ (528 points), and interestingly we could identify a number of specific BZ points, not yet probed by ARPES, where sizeable non-trivial temperature dependent renormalization effects are obtained.

Concretely, in Figure 10(a) we exhibit the temperature dependence of the imaginary part of $\Sigma_c(k, \omega)$ at

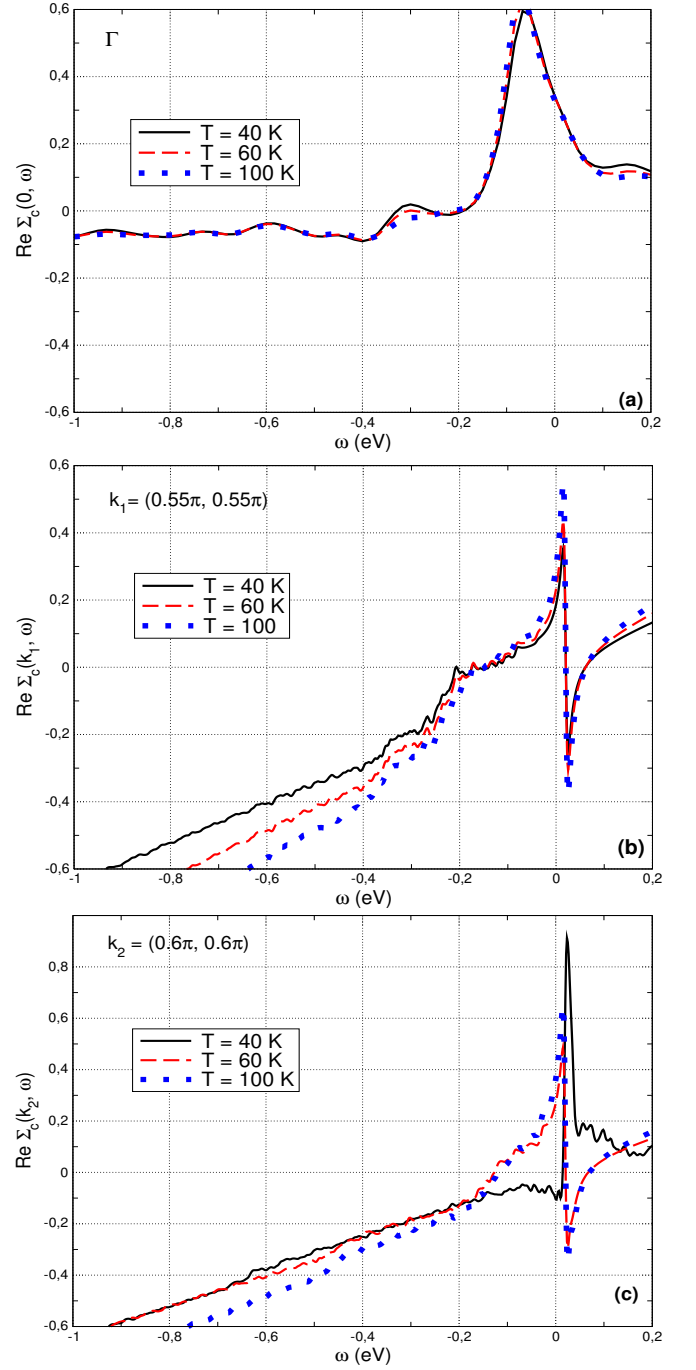


FIG. 11. Temperature dependence of the real part of $\Sigma_c(k, \omega)$ at the BZ points respectively indicated in the plots. T as labelled in the figure, other parameters as in Fig. 8.

$\vec{k} = (0.55\pi, 0.55\pi)$: a BZ point where we find that, increasing temperature, interaction-related renormalization effects lead to a redistribution of spectral weight near the Fermi level, with temperature dependent peaks evolving in the energy range $[-0.4, -0.2]$ eV.

In Figure 10(b), we exhibit the temperature dependence of the imaginary part of $\Sigma_c(k, \omega)$ at $\vec{k} =$

$(0.6\pi, 0.6\pi)$, where the spectral weight redistribution is even larger, involving e.g. a number of states present above the Fermi level at $T=40\text{K}$, which are pushed below the Fermi level at higher temperatures, leading to a number of peaks with temperature-dependent location and height in the energy range $[-0.7, 0]$ eV.

Finally, in Figure 10(c) we exhibit the temperature dependence of the imaginary part of $\Sigma_c(k, \omega)$ at $\vec{k} = (0.56\pi, 0.31\pi)$. Notice that, increasing temperature, the interaction effects lead to temperature dependent peaks now in the energy range $[-0.6, -0.1]$ eV. It would certainly be interesting to investigate these predictions by ARPES.

b. Real part of the self-energy

To complete the presentation of the renormalization effects described in our approach, in Figure 11 we show the evolution with temperature of the real part of $\Sigma_c(k, \omega)$ at the BZ centre, where it is negligible, and at two of the k-points we identified as having relevant non-trivial temperature dependence, discussed above. The results in Fig. 11 are the Kramers-Kronig related counterparts of the imaginary part of the self-energies shown in Figs. 9, 10(a) and 10(b) respectively. We checked that the renormalizations at M and X , as expected, are almost independent of temperature.

Appendix C: Description of doping effects on the electronic structure

Here, we complement our discussion of the effects of doping on the electronic structure of Section 3.3, mainly presenting spectral density function results. In particular, we analyze the main changes in $\tilde{A}(\vec{k}, \omega)$ with doping, fixing \vec{k} at the relevant high-symmetry points of the BZ which were experimentally studied. We compare with ARPES[76] and angle integrated valence band photoemission experiments[77] on undoped, Co-doped (electron doped), and K-doped (hole doped) Ba-122 single crystals, in which asymmetric electron-hole doping effects on the electronic structure were reported,[76,77] confirming previous indications of Hall and transport experiments.[79]

In Fig. 12, we show $\tilde{A}(\vec{k}, \omega)$ for three cases, corresponding to the fillings of the Ba-122 compounds studied in Refs.[76,77]: the undoped ($n = 2$), hole-doped ($n = 1.85$), and electron-doped ($n = 2.25$) systems. at the Γ and M Brillouin zone points. As observed at Γ with ARPES,[77] we obtain two main peaks (apart from a few other peaks all of lower intensity): one of them centered at binding energy 0.55 eV for the undoped compound, and the other one near the Fermi level, which shift their positions according to doping following the trend observed in experiments. Concretely, the peak at $\omega \sim -0.55$ eV for the undoped system, appears

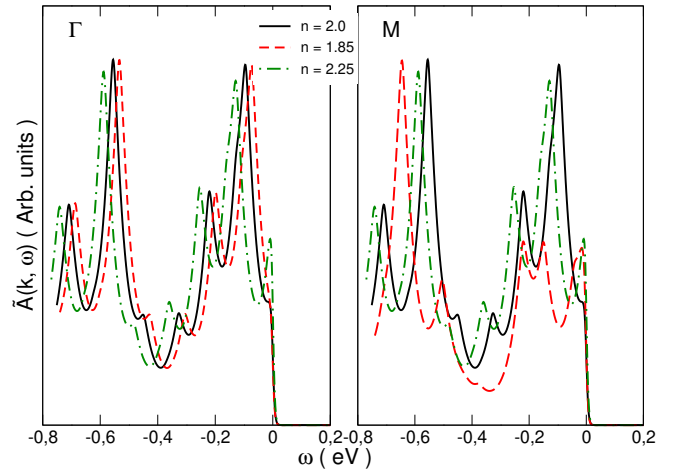


FIG. 12. Comparison of the effect of electron vs. hole doping on $\tilde{A}(k, \omega)$, at Γ and M points. $T = 40\text{K}$, $U = V = 3.50\text{eV}$, $\nu = 9$. Other parameters as in Fig.1.

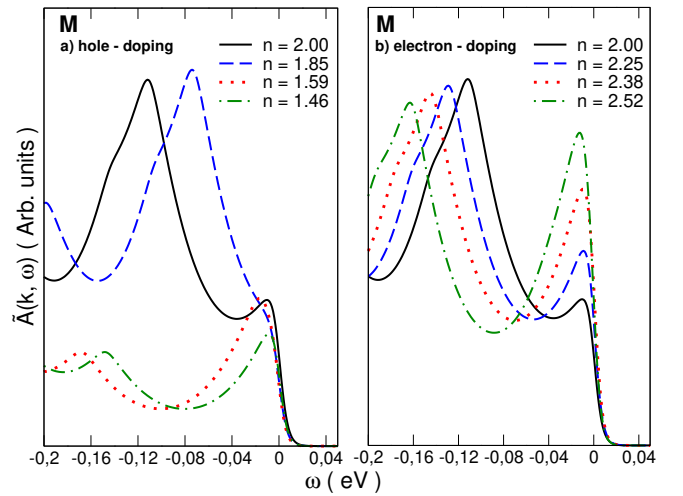


FIG. 13. Effect of a) hole doping and b) electron doping on $\tilde{A}(k, \omega)$, at M point. $T = 40\text{K}$, $U = V = 3.50\text{eV}$. $\nu = 9$. Other parameters as in Fig.1.

shifted away from the Fermi level: at $\omega \sim -0.60$ eV for the electron-doped system, while for the hole-doped system it appears shifted in the opposite direction: at $\omega \sim -0.50$ eV. In fact, at Γ the whole spectrum appears shifted analogously as a function of doping. Thus, electron-hole asymmetric effects such as experimentally observed[76,77] are present in the renormalized electronic structure of our model. Regarding the spectral densities at M shown in Fig. 12, the situation is seen to differ: though the same trend of spectral weight shifts upon doping sign is seen for the part of the spectrum corresponding to energies closer to the Fermi level ($\omega > -0.4$ eV), an important spectral weight redistribution is also present upon doping.

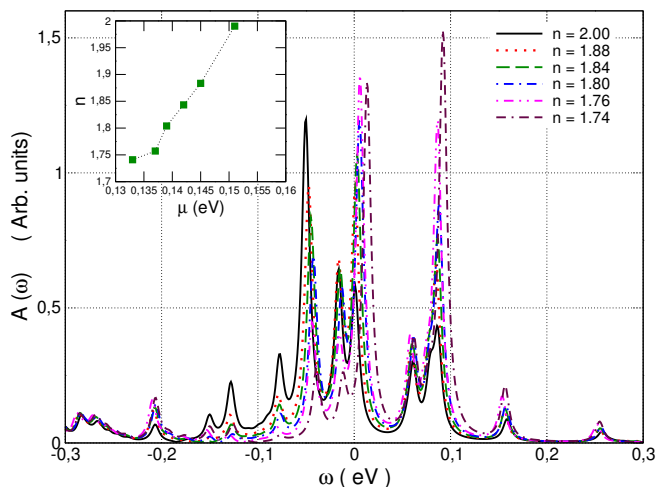


FIG. 14. Total DOS $A(\omega)$, for different values of **hole** doping (indicated in the figure) at $T = 20$ K, $U = V = 3.50$ eV. Other parameters as in Fig.1. Inset: dependence of the chemical potential on total band filling.

In Fig. 13 we focus on the spectral density at M in the range of energies closer to the Fermi level studied by ARPES in Ref.[76], and exhibit our results for more values of charge doping: (a) for hole doping, and in (b) for electron-doping. The nature of the spectral weight redistribution that we find takes place upon doping is in qualitative agreement with the reported data.[76] Increasing hole-doping, spectral weight from lower energies is transferred towards the Fermi level. Meanwhile, increasing electron doping we obtain a smooth increase of the quasiparticle weight at the Fermi level, while other states are pushed away to lower energies.

In Figure 14 we complement the results presented in Fig. 3, showing the total DOS for a larger number of hole doping values. One clearly appreciates that increasing hole-doping, a rigid-band-like shift of all peaks towards the Fermi level is obtained, thus increasing spectral weight there in agreement with ARPES results on doped BaFe_2As_2 ,[76] where a smooth chemical potential shift upon doping, related to the effective masses of the low-energy valence states, was observed. The filling-dependence of the chemical potential in our model is shown as an inset in Fig. 14.

Finally, in Figure C.8 we exhibit effects of doping on the renormalized Fermi surface (FS) topology of the correlated two-orbital model. Notice that several Lifshitz transitions are obtained. Starting from the FS typical of parent compounds ($n = 2$), doping with electrons mainly

reduces the hole point around the BZ centre Γ , until it disappears at critical electron filling $n_e \sim 2.65$. At the same time, one can see that electron doping increases the four electron pockets located around the BZ points: X,Y, -X,-Y, until a new FS topology emerges at n_e , with a larger electron FS around Γ . This is qualitatively consistent with experimental reports [22,23]. Similarly, notice in Figure C.8 that hole doping reduces the four above-mentioned electron pockets until at critical hole filling $n_h \sim 1.81$ they disappear, and a new FS topology emerges: only consisting of the hole pockets.

1. Temperature dependence of the electronic structure: effect of doping.

After having discussed in section 3.4 the effects of temperature on the electronic structure for the parent compounds ($n = 2$), here we compare them with the results predicted for doped systems.

In Figure C.9 we focus on the total density of states: the results shown evidentiate that the non-trivial temperature dependent renormalization effects by correlations found for the parent compounds, shown in Fig. C.9.(b) and previously discussed in connection with Figure 4, are greatly reduced when doping is introduced. In particular, Fig.C.9.(a) shows that for hole doping, increasing temperature, the dominant peak near the Fermi level is not displaced and the main effect of temperature is the usual expected thermal broadening (and consequent decrease of the height of the peak). While for electron-doping, Fig.C.9.(c) shows that a certain non-trivial redistribution of spectral weight still appears with temperature, though much less important than for the parent compounds: notice that the dominant peak near the Fermi level, is shifted to lower energies by an increase of temperature, reducing its height.

We also explored the effect of doping on the temperature dependent spectral density function results. In Figure C.10, for an electron-doped system, we focus on the spectral density function: in particular for the three Brillouin zone points previously discussed in connection with Figure 6, exemplifying BZ points we could identify for the parent compounds where larger non-trivial temperature dependent renormalization effects by correlations are predicted. Notice that doping strongly affects those k-dependent results: for the two BZ points shown in Figs. C.10.(a) and C.10.(c), the presence of doping has suppressed the temperature dependence. While Fig. C.10.(b) shows that for $\vec{k}_2 = (0.6\pi, 0.6\pi)$ some temperature dependence is still retained. For hole doping, we found that no relevant temperature dependent effects are retained at these three BZ points.

¹ Y. Kamihara et al., J. Am. Chem. Soc. 130, 3296 (2008).

² J. Paglione, R. L. Greene, Nature 6, 645 (2010).

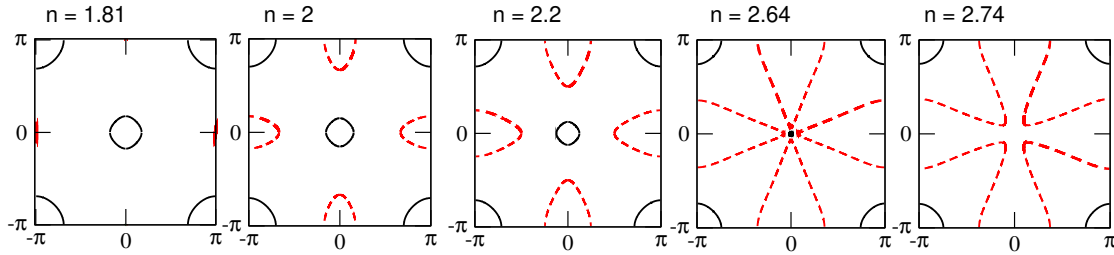


FIG. 15. Correlated two-orbital model: doping evolution of the (large) Fermi surface (one Fe atom / cell), at $T = 40$ K. Electron- (dashed) and hole pockets (solid lines), at five indicated fillings ($n = 2$: parent compound). Parameters: $U = V = 3.5eV$, tight-binding parameters from Ref.[30]

- ³ X. Zhu et al., Phys. Rev. B 79, 024516 (2009).
- ⁴ H. Hosono and K. Kuroki, Physica C 514, 399 (2015).
- ⁵ For a review on itinerant model based studies, see Nan Lin Wang, Hideo Hosono, Pengcheng Dai (Eds.), Iron-based Superconductors: Materials, Properties and Mechanisms, Pan Stanford Publishing, 2013 (Chapter 8).
- ⁶ For a review on the gap symmetry, see P.J. Hirschfeld, M.M. Korshunov, I.I. Mazin, Rep. Prog. Phys. 74, 124508 (2011).
- ⁷ D. J. Scalapino, Rev. Mod. Phys. 84, 1383 (2012).
- ⁸ S. Lebegue, Phys. Rev. B 75, 035110 (2007).
- ⁹ Y. Kamihara et al., J. Am. Chem. Soc. 128, 10012 (2006).
- ¹⁰ D. J. Singh and M.-H. Du, Phys. Rev. Lett. 100, 237003 (2008).
- ¹¹ L. Craco et al., Phys. Rev. B 78, 134511 (2008).
- ¹² I. I. Mazin et al., Phys. Rev. B 78, 085104 (2008).
- ¹³ D.J. Singh, Phys. Rev. B 78, 094511 (2008).
- ¹⁴ D. J. Singh, Physica C 469,418 (2009).
- ¹⁵ L. X. Yang et al., Phys. Rev. B 82, 104519 (2010).
- ¹⁶ L. X. Yang et al., Phys. Rev. Lett. 102, 107002 (2009).
- ¹⁷ C. He, Y. Zhang, B. P. Xie, et al., Phys. Rev. Lett. 105, 117002 (2010).
- ¹⁸ Y. Zhang, F. Chen, C. He, et al., Phys. Rev. B 82,165113 (2010).
- ¹⁹ F. Chen, B. Zhou, Y. Zhang, et al., Phys. Rev. B 81, 014526 (2010).
- ²⁰ H. Ding et al., J. Phys.: Condens. Matter 23, 135701 (2011).
- ²¹ M. G. Holder et al., Phys. Rev. B 86, 020506(R) (2012).
- ²² Chang Liu, A.D. Palczewski, R.S. Dhaka et al., Phys. Rev. B. 84, 020509 (2011).
- ²³ S.T. Cui, S.Y. Zhu, A.F. Wang et al., Phys. Rev. B. 86, 155143 (2012).
- ²⁴ I. Nekrasov et al., JETP Lett. 87, 560 (2008)/ JETP Lett. 88, 144 (2008).
- ²⁵ A. I. Coldea et al., Phys. Rev. Lett. 101,216402 (2008).
- ²⁶ P. Vilmercati et al., Phys. Rev. B 79, 220503 (R) (2009).
- ²⁷ S. Thirupathaiah et al., Phys. Rev. B. 81, 104512 (2010).
- ²⁸ V. Zabolotnyy et al., Physica C 469, 448 (2009).
- ²⁹ C. Liu et al., Phys. Rev. Lett. 102, 167004 (2009).
- ³⁰ S. Raghu, X.-L. Qi, C.-X. Liu, D. J. Scalapino, and S.-C. Zhang, Phys. Rev. B 77, 220503(R) (2008).
- ³¹ Zi-Jian Yao, Jian-Xin Li and Z. D. Wang, New J. Phys. 11, 025009 (2009).
- ³² S. Graser et al., New J. Phys. 11, 025016 (2009).
- ³³ J. Hu, and N. Hao, Phys. Rev. X 2, 021009 (2012).
- ³⁴ G.-K. Liu et al., J. Phys. Cond. Matt. 26, 325601 (2014).
- ³⁵ Y. Zhou, D. Xu, F. Zhang and W.Chen, Europhys. Lett. 95, 17003 (2011).
- ³⁶ Y. Ran et al., Phys. Rev. B 79, 014505 (2009).
- ³⁷ E. Dagotto et al., Front. Phys. 6(4), 379 (2011).
- ³⁸ A. Ptok, D. Criwelli, and K. Kapcia, Supercond. Sci. Technol. 28, 045010 (2015).
- ³⁹ A. Akbari, I. Eremin, and P. Thalmeier, Phys. Rev. B 84, 134513 (2011).
- ⁴⁰ R.Yu, J. Zhu, and Qimiao Si, Phys. Rev. Lett. 106, 186401 (2011).
- ⁴¹ R. Yu, and Qimiao Si, Phys. Rev. B 84, 235115 (2011).
- ⁴² T. Yamada, J. Ishizuka and Y. Ono, J. Phys. Soc. Jpn. 83, 044711 (2014).
- ⁴³ M. J. Calderón et al., New J. Phys. 11, 013051 (2009).
- ⁴⁴ A. Aperis et al., Phys. Rev. B 83, 092505 (2011).
- ⁴⁵ D. Y. Liu et al., Phys. Rev. B 84, 064435 (2011).
- ⁴⁶ T. Miyake et al., J. Phys. Soc. Jpn. 77, 99 (2008).
- ⁴⁷ K. Haule, J. H. Shim, and G. Kotliar, Phys. Rev. Lett. 100, 226402 (2008).
- ⁴⁸ M. S. Laad, and L. Craco, Phys. Rev. Lett. 103, 017002 (2009).
- ⁴⁹ S.L. Skornyakov et al., Phys. Rev. B 81, 174522 (2010).
- ⁵⁰ S.L. Skornyakov et al., Phys. Rev. Lett. 106, 047007 (2011).
- ⁵¹ S.L. Skornyakov et al., Phys. Rev. B 86, 125124 (2012).
- ⁵² A. Shorikov et al., J. Exp. Theor. Phys. 108, 121 (2009).
- ⁵³ L. Craco, M. S. Laad and S. Leoni, Phys. Rev. B 84, 224520 (2011).
- ⁵⁴ T. Terashima et al., J. Phys. Soc. Jpn. 79, 053702 (2010).
- ⁵⁵ T. Yoshida et al., J. Phys. Chem. Solids 72, 465 (2011).
- ⁵⁶ D. H. Lu et al., Nature 455, 81 (2008).
- ⁵⁷ H. Liu et al., Phys. Rev. B 78, 184514 (2008).
- ⁵⁸ S. E. Sebastian et al., J. Phys. Condens. Matter 20, 422203 (2008).
- ⁵⁹ J. G. Analytis et al., Phys. Rev. Lett. 103, 076401 (2009).
- ⁶⁰ T. Kroll et al., Phys. Rev. B 78, 220502 (2008).
- ⁶¹ W. L. Yang et al., Phys. Rev. B 80, 014508 (2009).
- ⁶² L. Ortenzi et al., Phys. Rev. Lett. 103, 046404 (2009).
- ⁶³ M. Daghofer et al., Phys. Rev. B 81, 014511 (2010).
- ⁶⁴ K. Kuroki et al., Phys. Rev. Lett. 101, 087004 (2008).
- ⁶⁵ D. H. Lu et al., Physica C 469, 452 (2009).
- ⁶⁶ Xiang Hu, C. S. Ting, and Jian-Xin Zhu, Phys. Rev. B 80, 014523 (2009).
- ⁶⁷ D. N. Zubarev, Sov. Phys. Usp. 3, 320 (1960).
- ⁶⁸ W. Nolting, *Fundamentals of Many-Body Physics*, translated by W. D. Brewer (Springer - Verlag Berlin Heidelberg

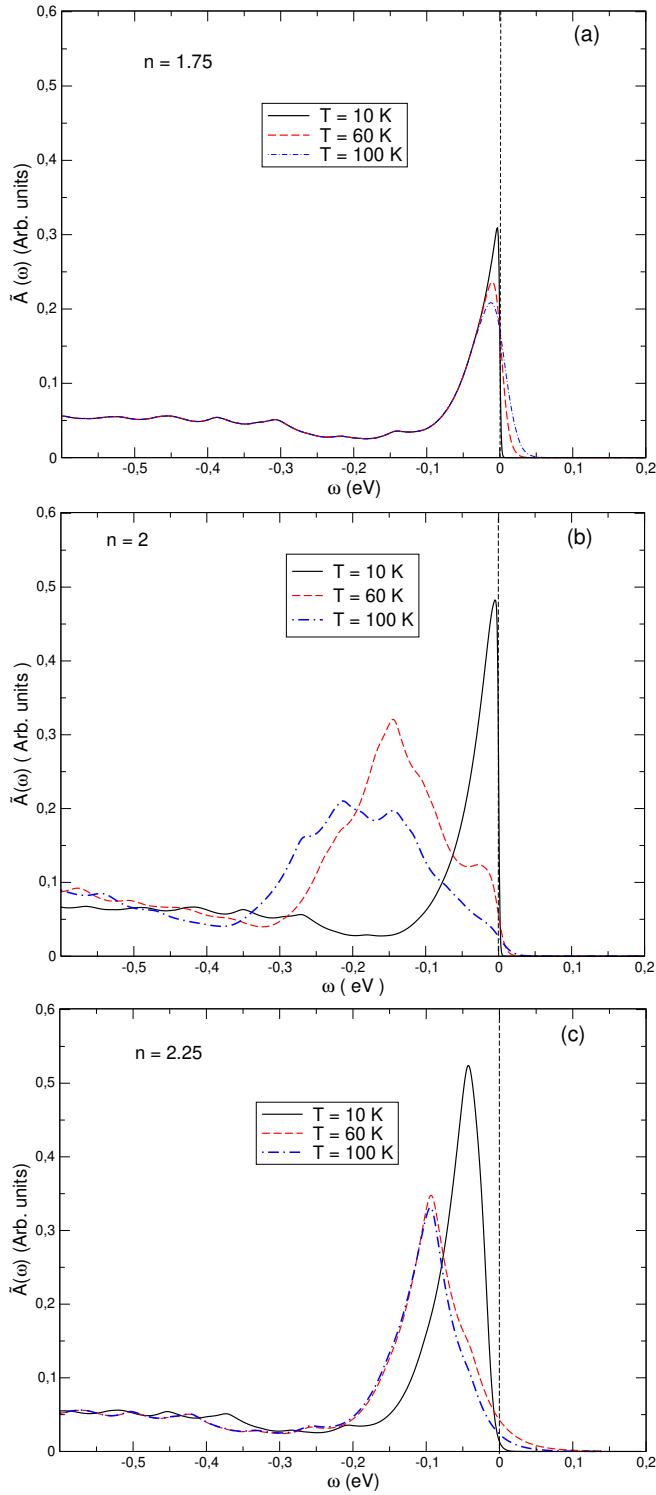


FIG. 16. Total DOS $\tilde{A}(\omega)$ shown at three temperatures: $T = 10$ K, 60 K and 100 K, for fillings: (a) $n = 1.75$ corresponding to hole-doping; (b) $n = 2$ (parent compounds); (c) $n = 2.25$ corresponding to electron-doping. $U = V = 3.5\text{eV}$, $\nu = 8$. Other parameters as in Fig.1.

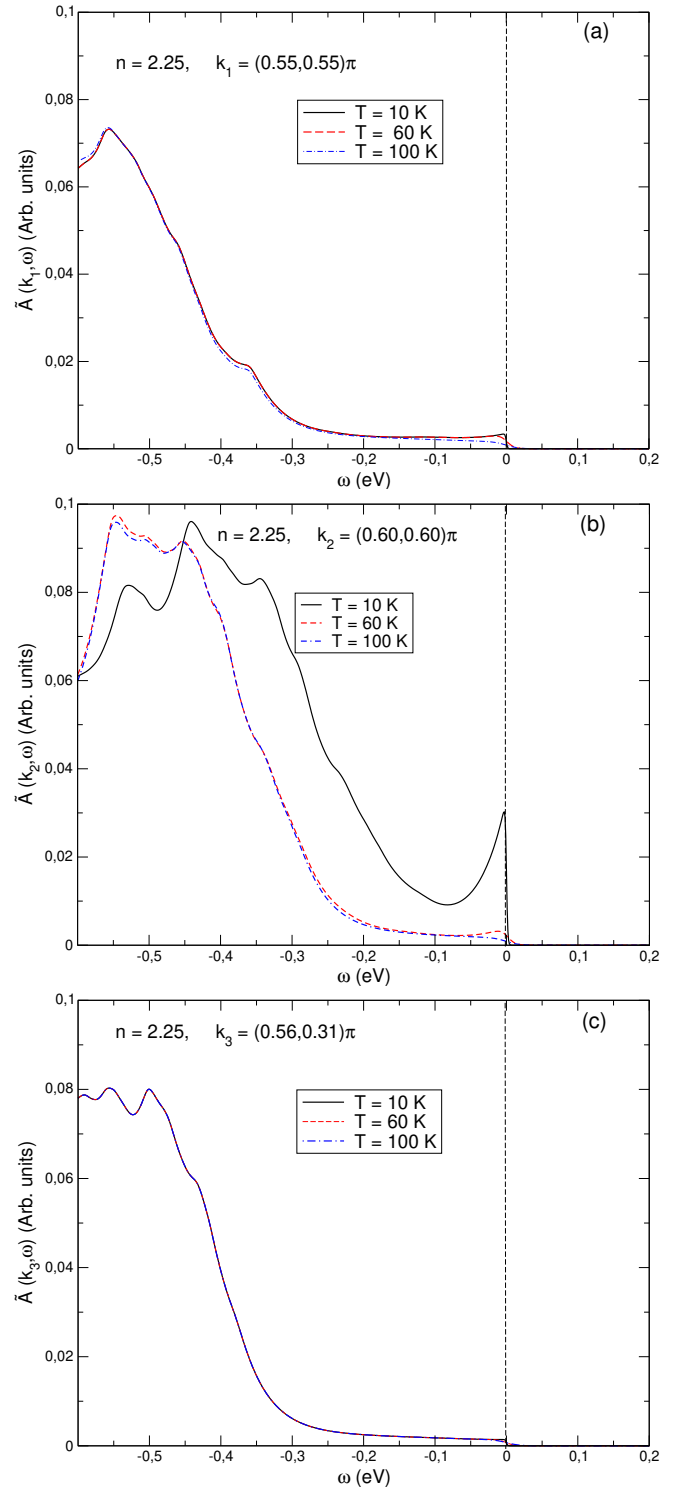


FIG. 17. Temperature dependence of $\tilde{A}(k, \omega)$ for $n = 2.25$: shown at three BZ points, respectively indicated in each plot. Parameters: $U = V = 3.5\text{ eV}$, $\nu = 8$. Other parameters as in Fig.1.

2009).

⁶⁹ L. M. Roth, Phys. Rev. 184, 451 (1969).

⁷⁰ L. Macot and B. Frank, Phys. Rev. B 41, 4469 (1990).

- ⁷¹ E. Z. Kurmaev et al., Phys. Rev. B 78, 220503(R) (2008).
⁷² H. Liu et al., Phys. Rev. Lett. 105, 027001 (2010).
⁷³ M. Yi et al., Phys. Rev. Lett. 110, 067003 (2013).
⁷⁴ Y. Sekiba et al., New Journal of Physics 11, 025020 (2009).
⁷⁵ K. Nakayama et al., Phys. Rev. Lett. 113, 237001 (2014).
⁷⁶ M. Neupane et al., Phys. Rev. B 83, 094522 (2011).
⁷⁷ S. Thirupathaiah, PhD Thesis in Physics, Tech. Univ. of Berlin (2011).
⁷⁸ Lei Fang et al., Phys. Rev. B 80, 140508 (R) (2009).
⁷⁹ H. Ding et al., Europhys. Lett. 83, 47001 (2008).
⁸⁰ K. Terashima et al., Proc. Natl. Acad. Sci. USA 106, 7330 (2009).
⁸¹ S. de Jong et al., Phys. Rev. B. 79, 115125 (2009).
⁸² J. Maletz et al., Phys. Rev. B 89, 220506(R) (2014).
⁸³ S. Thirupathaiah et al., Phys. Rev. B. 86, 214508 (2012).
⁸⁴ D. V. Evtushinsky et al., Phys. Rev. B. 87, 094501 (2013).
⁸⁵ B. Zhou et al., Phys. Rev. B. 81, 155124 (2010).
⁸⁶ L. Fanfarillo, and E. Bascones, Phys. Rev. B 92, 075136 (2015).
⁸⁷ S.D. Das, M.S. Laad, L. Craco et al., Phys. Rev. B 92, 155112 (2015).

